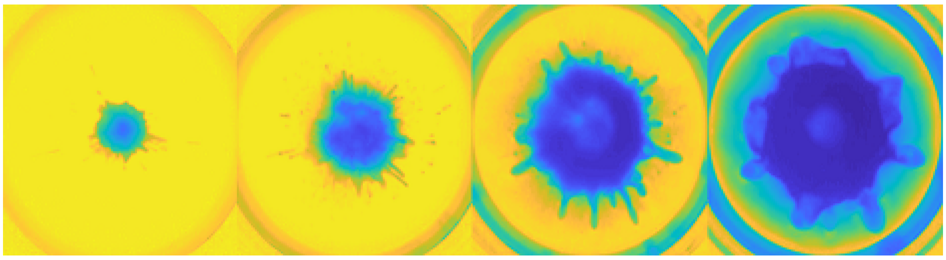

Nanofluid spray cooling characterization combining phase Doppler anemometry with high-speed visualization and thermography

Miguel Silva Figueiredo

Thesis to obtain the Master of Science Degree in

Mechanical Engineering

Supervisors: Prof. António Luís Nobre Moreira
Prof. Ana Sofia Oliveira Henriques Moita

Examination Committee

Chairperson: Prof. Edgar Caetano Fernandes
Supervisor: Prof. Ana Sofia Oliveira Henriques Moita
Member of the Committee: Prof. Miguel Rosa Oliveira Panão

October 2020

Acknowledgments

First, I would like to acknowledge my supervisor and teacher Doctor Ana Moita for her insight, knowledge and patience put into this dissertation. I would also like to acknowledge Professor Doctor Luís Moreira for accepting me into his laboratory team.

A big thanks to Pedro Pontes for his essential help when it comes to experimental knowledge, for his patience and friendship, without him this dissertation would be a lot harder.

A special thank to Professor Doctor Miguel Panão for the phase Doppler system explanations, and Doctor Ana Paula Ribeiro for the preparation of the nanofluids and explaining my doubts regarding the nanoparticles.

I would also like to acknowledge my friends and colleagues at the boiling laboratory who directly or indirectly helped me to complete this dissertation. Thank you for all the jokes, friendship and for the coffee breaks.

Finally, I would like to sincerely acknowledge my parents and sister, for their guidance, encouragement and unconditional support. Additionally, I would like to thank my cousins, especially to João, for helping me with this dissertation writing.

Last but not least, I would like to thank my girlfriend, for her company, love and support.

Abstract

The spray-wall interactions depict thermo fluid dynamics phenomena exploited in a vast range of applications, from internal combustion engines, electronic components cooling, HVAC, to numerous medical and industrial applications. Additionally, climate change awareness cries for the urgent development of more efficient and more climate-friendly cooling systems. For these reasons, the scientific community has been showing an interest in uncovering nanofluid possible applications. As they possess superior thermal conductivity and overall better thermal cooling performance, their potential use as a coolant has become a great promise.

In this order, nanofluids with gold and silver nanoparticles, with different geometries and concentrations ranging from 0.1 - 1 (wt.%) were atomized and characterized. The study performed on this dissertation adopted a novel combination of three techniques little exploited in the literature. The phase Doppler anemometry system and the synchronization of a high-speed camera with a high-speed thermographic infrared camera were used to describe spray impact onto the heated surface.

According to the results, a decreased surface tension and higher impingement distance favour heat transfer from the wall, as the wetted area increased. Moreover, changes in the thermophysical properties were noted with the addition of nanoparticles, when compared to the base fluid. Although their presence did not affect the spray dynamics, an increase of 9.8% to 21.9% of the maximum heat flux was noted during impact when compared to the base fluid.

Keywords

Spray cooling, Nanofluid, Time Resolved Infrared Thermography, Phase Doppler Anemometry.

Resumo

A interação entre spray e superfície retrata fenómenos termofluido-dinâmicos presentes em várias aplicações práticas, desde motores de combustão interna, arrefecimento de componentes eletrónicos, ventilação e sistemas AVAC, incluindo várias aplicações médicas e industriais. Adicionalmente, com a crescente consciencialização da situação ambiental atual, nota-se uma ascendente preocupação no desenvolvimento de sistemas de remoção de calor mais eficientes. Por estas razões, nos últimos anos, tem havido um interesse pela comunidade científica no escrutínio de possíveis aplicações de nanofluidos. A sua aplicação como refrigerantes, tem vindo a revelar-se como uma grande promessa em remover elevadas cargas de calor, graças às suas propriedades termodinâmicas superiores.

Neste sentido, nanofluidos com nanopartículas em ouro e prata, com diferentes geometrias e com concentrações entre 0.1 - 1 %(m/m) foram atomizados e caracterizados. Nesta dissertação a combinação de três técnicas de análise, pouco explorada na literatura, foi adotada. Deste modo, recorreu-se à anemometria de laser doppler e ao sincronismo de uma câmara de alta velocidade com uma câmara termográfica de infravermelhos, para descrever em detalhe o impacto de sprays numa superfície aquecida. De acordo com os resultados obtidos, a baixa tensão superficial e maior altura de impacto favoreceram a remoção de calor da superfície, visto que aumentam o crescimento da área molhada. Quanto à adição de nanopartículas, notaram-se alterações nas propriedades termofísicas em relação ao fluido base. No entanto, estas não influenciaram a dinâmica do spray, mas resultaram num aumento de 9.8% até 21.9% no fluxo de calor máximo, quando comparados ao fluido base.

Palavras Chave

Arrefecimento de Sprays, Nanofluidos, Termografia de Infra Vermelhos com Elevada Resolução Temporal, Anemometria de Laser Doppler.

Contents

List of Figures

List of Tables

Acronyms

ADU	Analog-Digital Units
CHF	Critical Heat Flux
CTAB	Cetyltrimethylammonium Bromide
DI	Deionized
HT	Heat Transfer
HTC	Heat Transfer Coefficient
MIN	Minimum Heat Flux
ONB	Onset of Boiling
PDA	Phase Doppler Anemometer
SCA	Spray Cone Angle
SMD	Sauter Mean Diameter

List of Symbols

A_s	Surface area	m^2
c_p	Specific heat	$J/(kgK)$
D	Droplet diameter	μm
D_0	Droplet initial diameter	μm
D_{10}	Mean droplet diameter	μm
D_{32}	Sauter mean diameter	μm
D_{43}	Brouckere mean diameter	μm
$D_{v0.1}$	10% fractional volume diameter	μm
$D_{v0.5}$	50% fractional volume diameter	μm
$D_{v0.9}$	90% fractional volume diameter	μm
E_r	Relative error	%
f_r	Fraction between the projected area and the wetted area by the liquid	-
h	Area-averaged heat transfer coefficient	μm
h_f	Liquid Layer Thickness	μm
I	Electrical current	A
k	Thermal conductivity	$W/(mK)$
K_c	Splashing parameter	-
L	Surface length	m
La	Laplace number	-
l_r	Length scale roughness	μm
n	Shape factor	-
N_p	Refractive index of the prim glass	-
N_s	Sample refractive index	-
Oh	Ohnesorge number	-
P	Power input	W
q''	Heat flux	W/m^2
q''_0	Imposed heat flux	W/m^2
r_f	Roughness factor	-
r	Radial position from the nozzle	mm
r^*	Dimensionless radial position from the nozzle	-
R	Electrical resistance	Ω
R_a	Average surface roughness	μm
R_D	Dimensionless roughness	-
Re	Reynolds number	-
S	Surface area of the particle	m^2
S'	Surface area of a an equivalent spherical particle with the same volume	m^2
$Span$	Distribution span	-
t	Time	ms

T^*	Dimensionless temperature	-
T_0	Initial Temperature	$^\circ C$
T_{CHF}	Critical Heat Flux temperature	$^\circ C$
$T_{Leindenfrost}$	Leindenfrost temperature	$^\circ C$
T_{local}	Local temperature	$^\circ C$
$T_{threshold}$	Threshold temperature	$^\circ C$
T_{sat}	Saturation temperature	$^\circ C$
T_w	Wall temperature	$^\circ C$
U	Axial velocity component	m/s
W	Surface width	m
We	Weber number	-
x	Cartesian coordinate	m
y	Cartesian coordinate	m
Z	Normal distance from the nozzle	mm

Greek symbols

α	Spray cone angle	$^\circ$
δ	Surface thickness	m
$\delta\alpha$	Spray cone angle absolute error	$^\circ$
δ_f	Dimensionless liquid film thickness	-
δT	Temperature absolute error	$^\circ C$
Δt	Time interval	ms
ΔT_e	Excess temperature	$^\circ C$
ϵ	Emissivity	-
θ	Static contact angle	$^\circ$
θ_y	Young angle	$^\circ$
μ	Dynamic viscosity	Kg/m^2s
ρ	Specific mass	Kg/m^3
ρ'	Electrical resistivity	Ω/m
σ	Surface tension	N/m
σ_{ls}	Surface tension at the liquid-solid interface	N/m
σ_{lv}	Surface tension at the liquid-vapour interface	N/m
σ_{sv}	Surface tension at the solid-vapour interface	N/m
ϕ	Volume fraction	-
ϕ_s	Scale reading	$^\circ$

1

Introduction

Contents

1.1 Motivation

Over the last few years, the development of the electronic systems, mainly in processing electronics, urges for the development of high heat flux removal systems. Cooling systems must assure the good functioning and endurance of these systems that are becoming more power concentrated due to aggressive miniaturization. The use of liquids has become an inevitable response, whether in single or two-phase liquid cooling, as heat dissipation from supercomputer chips approached 100 W/cm^2 [1, 5].

The most used liquid cooling systems come from pool boiling, channel or microchannel flow boiling, jet-impingement and spray cooling. Each approach has its advantages, nevertheless, spray cooling is considered by some as the most advantageous (e.g. [5]). In ideal conditions, spray cooling achieves a heat flux removal in the order of 1200 W/cm^2, an order of magnitude higher than pool boiling, which only achieves 140 W/cm^2. When compared with jet-impingement, spray cooling offers better spatial cooling uniformity, that otherwise would be detrimental to some devices, resulting in higher cooling efficiencies and lower liquid consumption [1, 6].

Spray cooling includes liquid and droplet-wall interactions that are governed by complex thermophysical phenomena, present in many practical applications, from internal combustion engines, microelectronics cooling, ventilation, to HVAC systems. Cases of interest also include numerous medical and industrial applications, that are guaranteed as a today standard [7–9].

In a simple way, spray cooling is obtained by the impact of the spray on the surface/element to cool. The spray is globally composed by numerous droplets within a wide range of sizes and velocities, which are generated at the nozzle, where the liquid breaks up due to instabilities, caused by its momentum. A spray, however, cannot be simply modelled as a sum of individual droplets, since there are numerous interactions between the droplets, with the air, and at impact with droplets previously spread on the surface as well as with a possible deposited liquid film, also resulting from earlier spray injection. However, spray cooling, due to its complexity, still lacks theoretical modelling when compared to other cooling techniques. Moreover, it is considered that spray cooling is limited by the cooling effectiveness of the conventional refrigerants, such as water, engine oil or ethylene [10].

Therefore, large interest by the scientific community regarding the scrutiny of nanofluid applications in cooling over the last few years is easily noticed. These nanofluids come with the promise of achieving higher heat transfer efficiencies, due to their enhanced thermal conductivity, when compared with conventional cooling fluids, whose properties largely enhance their cooling performance [8, 11].

Nanofluids are composed of solid particles that are dispersed in a base liquid (e.g. Deionized (DI) Water, Refrigerant Oils). These particles can be metallic (e.g. Aluminum, Gold, Silver) or nonmetallic (e.g. Carbon and Nitrides), whose dimensions are in the nanometer range (typically from 10 – 100 nm) [12]. Since nanoparticles have higher thermal conductivities, at least two orders of magnitude higher than their base liquid, they enhance the fluid's overall thermal conductivity. Additionally, other fluid-dynamic characteristics are stated in various studies, such as Brownian movement and higher fluid stability that should prevent particle settlement that, in theory, should enhance the flow and heat transfer processes [11].

Nevertheless, controversial conclusions regarding the increase of the thermal conductivity and its contribution to enhance or worsen heat transfer can be found in the literature. In one hand, this means that more studies and more detailed analysis are still needed [10, 11]. On the other hand, there are other properties such as viscosity and local wettability, which can be strongly affected by the addition of the nanoparticles to the base fluids, altering the hydrodynamic characteristics of the flow, in complex processes which are still far to be accurately described.

In this regard, to diminish the existing gaps in this topic, this study is aimed at correlating the nanoparticle presence in the base fluid and its effect on thermophysical properties. Therefore, its influence on the atomization process and heat transfer is analyzed at two impact distances and two initial surface temperatures. This study is a followup to a previous study [7], and it considers nanofluids with different nanoparticle chemical element, geometry and concentration. The atomization and heat transfer process are characterized using a novel combination of three techniques: the phase doppler anemometry and high-speed visualization imaging, coming from a high-speed camera and a thermographic camera.

1.2 State of the Art

Following the brief motivation provided in the previous subsection, the main goal of this segment is to give the reader the context of the present study in the wide range of experimental studies performed in spray cooling and nanofluid spray cooling of flat surfaces. Additionally, the definition of important parameters will be presented and discussed with more detail in Chapter 2.

Sprays come from the atomization process, that results from forcing a liquid to pass through a small aperture. It is composed of a wide range of droplet sizes, that will disperse and (assuming their cooling purpose) they will impact the surface to cool. During impact, large amounts of heat are removed from the surface, either by single-phase convection and sensitive heat, mainly through the liquid film motion that forms due to droplet build-up or by two-phase heat transfer, as nucleation sites start to form, hence taking advantage of the liquid latent heat [5]. According to Z. Yan (2011) [13], the main heat transfer mechanisms surrounding spray cooling are the evaporation of the liquid film, the forced convection that comes from droplet impinging and then spreading on the surface and nucleation enhancement on the surface. However, the mechanisms that lie under heat transfer during spray cooling depend on many factors. Therefore, it is a very challenging task to independently study some parameters without affecting others, as each spray nozzle produces different droplet sizes and velocity distributions that change with pressure drop or even with the working fluid.

Estes and Mudawar (1995) [14], performed experiments on the nucleate boiling regime for a full cone atomizer. An electrically heated small area with 12.7 mm in diameter with one thermocouple beneath it, was impinged with a dense spray. One-dimensional heat conduction was assumed, and a PDA was used for droplet sizing, at 45 mm from the nozzle tip. From their experiments, the nucleate boiling and single-phase heat transfer slopes showed less increase for high volumetric dense sprays than for lower volumetric ones. The authors attributed this behaviour to the lower evaporation efficiency and concluded that the Critical Heat Flux (CHF) increases for sprays with high flow rates and lower Sauter Mean Diameter (SMD). Later, Chen et al. (2002) [6], attributed that droplet velocity is the dominant effect on CHF, followed by droplet flux. So, to increase the CHF in spray cooling, a diluted spray with lower droplet size but with higher velocities is preferable to another denser spray with bigger droplet size and lower velocity.

In 2011, Cheng et al. [15], used a Phase Doppler Anemometer (PDA) to analyze DI Water spray characteristics when impinging a heated area with 12 mm in diameter. Spray height, liquid flow rate and liquid inlet temperature were varied. For Heat Transfer (HT) analysis, 4 layers of small thermocouples were used. As the spray flow rate increased, by increasing the pressure drop, the velocity and droplet number flux increased, as opposed to the SMD. This resulted in the overall HT increase. Moreover, it was observed that decreasing the impingement height, the HT increases. This last observation should be carefully interpreted, as the heated area was small compared to the spray dispersion area. Hence, only a fraction of the spray was effectively cooling the surface. This point of view was also postulated in [14], as the CHF should increase with impingement height until the impingement spray area reaches the heated surface limits. Nevertheless, the CHF increase with impingement height was attributed to the increased droplet splash on the surface, that enhances the fluid film discharge from the surface. This conclusion is somewhat contradicting, as enhancing splash should diminish the time of heat transfer between the surface and the splashing droplets.

Although these parametric studies in spray cooling are quite important, other authors are taking another approach, by changing the working fluid own thermophysical properties by adding nanoparticles to the base liquid, that changes its surface tension, viscosity, contact angle and, most importantly, the thermal conductivity [1]. In fact, according to M. Gupta (2017) [11], the thermal conductivity of nanofluids are in most cases higher than the base fluids. This can be attributed to two mechanisms, to Brownian motion of the nanoparticle suspensions, i.e. random motion of particles that induces convection, and to the formation of a nanolayer at the nanoparticle surface, that acts as a thermal bridge between the solid particle and the base liquid [11, 16]. Nevertheless, J. Philip (2012) [16] points out that the enhancement of the thermal conductivity relies on many factors like nanoparticle size, morphology, base material, pH, volume fraction and even base fluid, as it can be also deduced from the various experimental results of nanofluid application in spray cooling.

In 2012, T. Chang [17] analyzed the effect of increasing the nanoparticle volume fraction of alumina nanoparticles on spray heat transfer performance. Three different alumina concentrations (0.001%, 0.025, and 0.05%) were dispersed in water. An enhancement on the thermal conductivity was noted when increasing the nanoparticle concentration. Regarding the Heat Transfer Coefficient (HTC), nanofluids with lower concentrations showed an improvement of up to 11.5%, whereas the highest concentration showed a reduction of 2.6% when compared to the base fluid. To explain this behaviour, the author verified the presence of a nano-sorption layer at the surface, due to nanoparticle deposition, when using high volume-fraction nanofluid. This should preclude the convective heat transfer at the surface, which can hamper the formation of nucleation points. Hence, it was postulated that low volume-fraction nanofluids are more suitable for spray cooling, as most of the nanoparticles are washed away from the surface, preventing the formation of a nano-sorption layer.

Hsieh et al. (2015) [10], carried out studies using different types of nanoparticles while increasing their volume concentration in DI water, from 0.04% to 0.1%. A flat plate copper heater with 4 cm^2 was sprayed by a full cone nozzle at a spray height of 30 mm. It was observed that all nanofluids enhanced the HTC in the nucleate boiling regime, including the CHT, compared to that of DI Water. Additionally, as the concentration increased, the heat transfer also increased, which conflicts with the observations made by T. Chang [17]. The author also observed that the HT enhancement of the nanofluids was not mainly related with the increased thermal conductivity, but rather with the lowered the surface tension, that should enhance the surface wettability, and also with the size and shape of the nanoparticle, as nanofluids with lower nanoparticle size resulted in higher HT.

Similarly, in 2015, S. Ravikumar [18] studied the heat transfer enhancement for alumina-water nanofluids using an air-atomized spray, impinging a flat surface at over 900 °C. Coolants of alumina-water, with 0.1% volumetric concentration, with and without surfactant were used. According to the results, a faster shift from transition boiling to nucleate boiling was noticed with the presence of nanoparticles. Additionally, nanofluids with the presence of surfactant showed better heat transfer than those without it. This was justified by the lower surface tension caused by the presence of surfactants, that increases the wettability of the surface and enhances surface nucleation points. Therefore, it also triggers the vapour film instability.

Recently, in 2019, M. Malý [7] performed experimental studies on the effect of the nature and concentration of the nanoparticles, within a range of mass concentrations from 0.01% to 2%, dissolved in water-based solutions, on spray hydrodynamics. These nanofluids were atomized using a swirl nozzle. Their velocity and droplet distributions were characterized using a PDA, whereas, for the spray cone angle, a high-speed camera was used. It was observed that the liquid viscosity plays an important role in atomization primary breakup, followed by surface tension, that dominated the secondary breakup. In the tested conditions, although slight changes were observed in droplet size across the spray radial position, nanofluids did not affect the spray dynamic characteristics. These observations suggest that nanofluid spray cooling would mainly be affected by the nanofluid thermal properties, supposedly in a positive way, as the spray or droplet dynamics would not be affected.

Following this discussion, one can argue that there is a lack consensus between studies regarding the effects of nanoparticle presence in spray cooling and mainly because spray cooling depends on many parameters that cannot be fully described by the currently utilized analysis techniques. Thereby, studies combining different experimental approaches must be pursued, to have a bigger picture of what it is happening during spray cooling or why nanofluid spray cooling can, in some instances, favour heat transfer or, in other cases, worsen it.

1.3 Objectives

The present dissertation aims at obtaining a detailed and accurate description of the combined hydrodynamic and heat transfer processes which occur during nanofluids spray impact on a heated surface. The present work focuses on the effect of the nature and concentration of the nanoparticles in the thermophysical properties of the nanofluids and the governing processes occurring during spray impingement and explore the potential of the nanofluids as coolant. To achieve this objective, other important characterizations must be performed, namely:

- To characterize the nanofluid thermophysical properties and wettability when increasing nanoparticle concentration and material, since these parameters affect spray cooling performance;
- To study their effect on the spray morphology using high-speed imaging, to qualitatively identify changes on the spray breakup process before impact (e.g. spray cone angle) and also to evaluate changes in the droplet diameter and velocity distributions at two different axial distances, using Phase Doppler anemometry techniques;
- To study their effect in the heat transfer process during spray impingement using high-resolution time-resolved infrared thermography. This analysis is particularly challenging as it requires the development/adaptation of calibration and validation procedures specific to the complex flow in study.

Additionally, the effect of surfactant without nanoparticles is also evaluated, as it plays an important role in surface tension, which in turn strongly affects the atomization characteristics of the spray.

1.4 Organization of this manuscript

The present dissertation is organized in five chapters, including this introduction aimed at contextualizing the reader to the present topic of spray cooling with nanofluids and the used experimental techniques.

In Chapter 2, a review of the main concepts and physical phenomena are explained in more detail, to better understand how atomization and heat transfer occurs, combined with droplet impingement outcome predictions.

Chapter 3 provides a description of the experimental setup and measurement/data processing methodologies, whereas an uncertainty analysis is also provided.

In Chapter 4, the results are presented and discussed.

Finally, in Chapter 5, the conclusions are provided with future prospectives.

2

Theoretical Background

Contents

2.1 Atomization Basics

2.1.1 Introduction

The atomization process relies on the transformation of a bulk liquid into droplets, in surrounding gas. Nevertheless, sprays have a wide variety of applications in distinct areas such as industrial applications, agricultural purposes, medicine, spray painting, internal combustion engines, metallurgy's, and thermal management. As they increase the surface area of the liquid, the atomizers play a major role in attaining a high index of mixing and evaporation inside the internal combustion engine, diminishing pollutant emissions [2, 13].

The device used in the atomization process is commonly named atomizer or nozzle, where the jet or liquid sheet breaks into droplets due to the high kinetic energy of the liquid, that enters in contact with a stagnant, surrounding, gas. Due to the unpredictable nature of the atomization process, the spray is normally characterized by a wide range of droplet sizes, that will differ for different atomizers.

2.1.2 Atomizers

The atomizers are classified by the atomization strategy used to produce droplets, according to their function. Following [19], they can be classified according to their:

- Mass flow rate;
- Spray pattern;
- Spray cone angle;
- Spay impact;
- Droplet size.

Most of these parameters rely on the working fluid hydrodynamic properties, discharge coefficient or pressure drop and nozzle geometry. The spray pattern reveals the shape and profile of the atomized liquid distribution on the surrounding gas. Therefore, three main patterns arise like the full cone, hollow cone and flat fan, represented in Figure 2.1.

Nozzles can display a range of different geometries, such as twin-fluid, airblast, air-assist, flat fan, swirl and rotary nozzles. A detailed description of the different nozzle geometries is out of the scope of this dissertation. Nevertheless, the swirl nozzle will be discussed as it was employed in this work.

The swirl nozzle is normally composed by a swirl chamber, that imposes rotation and centrifugal forces on the incoming liquid. The liquid leaves through a small orifice as a liquid sheet with small rings, due to pressure differences, that end up breaking and generating small droplets. Additionally, this type

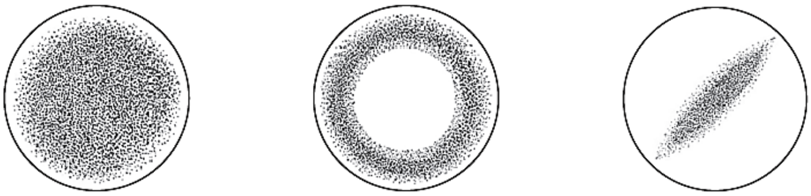

(a) Full Cone **(b)** Hollow Cone **(c)** Flat Fan

Figure 2.1: Different spray patterns. Adapted from [1]

of nozzle geometry normally generates a hollow cone spray, although a full cone is also possible, but less common.

Moreover, the Spray Cone Angle (SCA) (α) can be as high as 90° for swirl sprays, hence they end up covering a wide area with fine droplets. That is one of the main reasons why this type of geometry is more suitable for surface cooling. On the downside, due to their small internal passages, they can get easily clogged, [19] which is a big disadvantage when paired with nanofluids.

2.1.3 Liquid Sheet Breakup Process

Before generating droplets, the liquid is primarily a continuum liquid sheet, as already referred. Most of the existing models attempting to describe this process are based on the aerodynamic instability [19]. This assumes the propagation of small instabilities that are generated inside the swirl chamber, forming helical waves, causing liquid thickness variations. As they get amplified, as seen in Figure 2.2 the liquid sheet starts to break, forming ligaments, that end up breaking into droplets, commonly named primary breakup droplets [19].

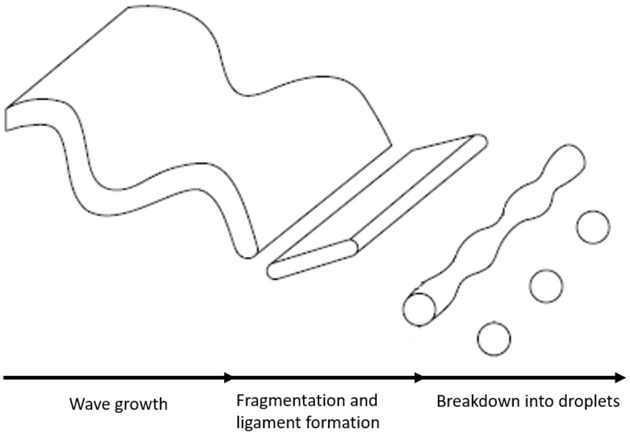

Figure 2.2: Liquid sheet breakup process. Adapted from [2]

According to some authors [2, 7], the atomization occurs under two distinct instances, forming the primary (already discussed) and secondary breakup droplets. The primary breakup arises directly from the sheet breakup and is directly influenced by the liquid's viscosity, since this property damps and retards instabilities amplification. This means that an increase in viscosity implies an increase of the liquid sheet breakup distance, increasing the overall droplet size. Additionally, surface tension plays also a major role in atomization, as it quantifies the forces that are needed to create a liquid surface area. It can also be defined as the minimum force needed to atomize a certain liquid.

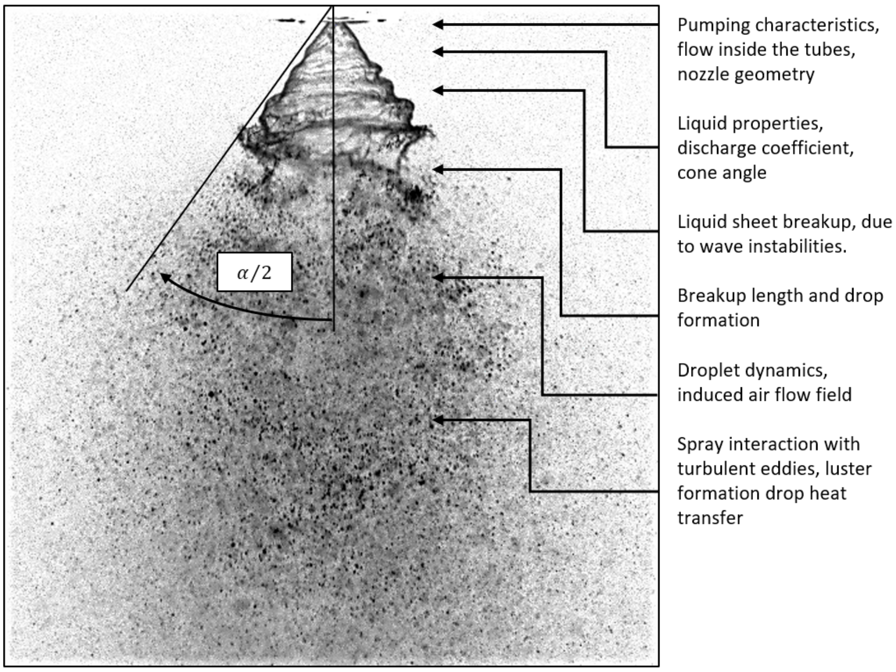

Figure 2.3: Swirl spray morphology description, according to [2]

Regarding the secondary breakup, it occurs much lower down the spray, where the interaction between droplets is intense, existing coalescence effects and droplet separation, as shown in Figure 2.3. Some authors suggest that the surface tension forces are governing the observed processes at this stage and viscosity variations play a secondary role [7].

2.2 Wettability Basics

Before referring to the impact criteria and the influence of nanoparticles on the base fluid, the concept of wettability is described.

Wettability is a thermodynamic property that quantifies the surface's tendency to get wet by a liquid, as a consequence of the equilibrium of the tensions at the liquid-gas-surface interface. It is mainly characterized by the contact angle, that is related to the equilibrium condition following the Young equation:

$$\sigma_{lv} cos\theta + \sigma_{ls} = \sigma_{sv} \tag{2.1}$$

where σ is the surface tension at the three interfacial boundaries (liquid-gas-solid surface) and the equilibrium contact angle, forming the equilibrium contact angle (θ).

Therefore, high wettable systems are associated with $0° < \theta < 90°$, and are named lyophilic (hydrophilic when the liquid is water), whereas low wettable systems with $90° < \theta < 180°$ and named lyophobic (hydrophobic when the liquid is water). Referring to the wettability extremes, complete wetting and non-wetting regimes correspond to $\theta = 0°$ and $\theta = 180°$, respectively.

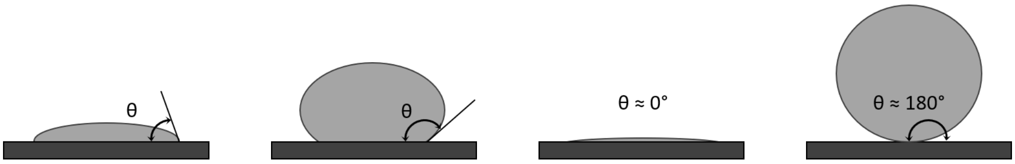

(a) Partial Wetting **(b)** Partial Non Wetting **(c)** Complete Wetting **(d)** Complete Non Wetting

Figure 2.4: Contact angles for different wettability regimes

Moreover, the contact angles do not depend only from the liquid and surrounding gas properties, but also from the surface geometry, topography and chemistry. Thus, the measured contact angles do not follow eq. (2.1), as the surface is not perfectly smooth. Therefore, two distinct situations arise:

- Homogeneous wetting: the liquid fully penetrates the air pockets, following the Wenzel's (1936) Equation (2.2):

  $$\cos\theta_{wz} = -r_f \cos\theta_y \tag{2.2}$$

  where r_f is the ratio between the actual surface area to its projected area.

- Heterogeneous wetting: the liquid does not fully penetrate these pockets, leading to air entrapment between the liquid and the surface, where Cassie and Baxter (1944) added the effect of the ratio of the projected area that is wetted to the total area (f_r), followed by Equation (2.3):

  $$\cos\theta_{CB} = -1 + f_r(r_f \cos\theta_y + 1) \tag{2.3}$$

2.3 Droplet/Spray Impact

2.3.1 Droplet Impact onto Non-heated Surfaces

The collision of a droplet onto a surface involves three different phases, related to the liquid (droplet), surrounding gas, and solid (target wall). These collisions can be described by different parameters that relate and combine physical properties and initial impact conditions, leading to different impingement outcomes.

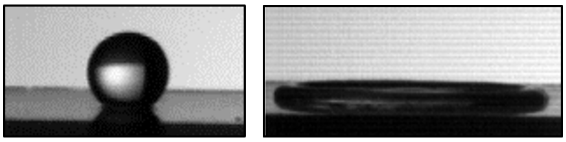

(a) Stick **(b)** Spread

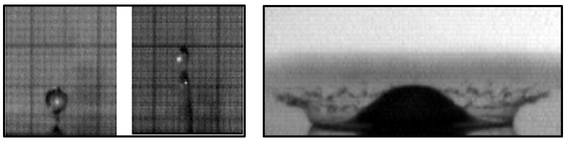

(c) Rebound **(d)** Splash

Figure 2.5: Basic impact outcomes from droplet impact. Adapted from [3].

Normally, these mechanisms or parameters are classified by the impact energy and the droplet morphology during impact. Bai et al. (1995) [20] considered four basic outcomes from droplet impact:

- Stick: the droplet softly adheres to the surface, nearly maintaining its spherical form. This outcome usually occurs at low Weber numbers ($We < 1$) (see Table 2.1 for the definition of the Weber number);
- Rebound: the droplet bounces back elastically (partially or totally) off the surface, after impact [21]. For cold surfaces, this only occurs for particular wetting conditions (hydrophobicity) or as a result of the interaction with a deposited liquid film on the surface;
- Spread: as the impact energy increases, the droplet adheres to the surface and spreads until its energy dissipates, forming a liquid film in the form of a lamella;
- Splash: the impact energy is high enough to form a crown after spreading. Normally, due to crown instabilities, it breaks and forms secondary droplets.

The splash regime can, in turn, be caused by different factors, hence different disintegration outcomes can be identified, as explained by Riobbo et al. (2001) [22]: prompt splash, corona splash, receding splash and partial rebound. More recently, Moita and Moreira (2007) [23] also identified the finger breakup, for non-wettable surfaces.

To summarise, the outcome of droplet impact relies on the combination of boundary conditions and droplet liquid properties and impact conditions, that lead to the development of empirical models to predict these outcomes. They relate the acting forces on the droplets, their physical properties (specific mass, viscosity and surface tension), diameter and velocity. Hence, they are grouped by the dimensionless numbers, showed in table 2.1.

Table 2.1: Dimensionless numbers affecting droplet impact

Dimensionless Numbers	Expression	Additional Relation	Physical Meaning
Reynolds number	$Re = \frac{\rho U D}{\mu}$		Ratio between inertial and viscous forces.
Weber number	$We = \frac{\rho U^2 D}{\sigma}$		Ratio between inertial and surface tension forces.
Ohnesorge number	$Oh = \frac{\mu}{\sqrt{\rho \sigma D}}$	$Oh = \frac{\sqrt{We}}{Re}$	Ratio between viscous and capillary forces.
Laplace number	$La = \frac{\rho \sigma D}{\mu^2}$	$La = \frac{1}{Oh^2}$	Ratio between surface tension and momentum forces.

2.3.2 Disintegration Limits

So, as aforementioned, the impact conditions affect the droplet impact outcomes. To establish the threshold criteria, distinguishing the different impact outcomes, empirical correlations were developed. Thresholds for the different regimes are usually defined in the literature. They rely on many parameters, as aforementioned, but also the surface roughness and temperature.

Most of these criteria were developed to establish a threshold between the occurrence of spread and disintegration. Therefore, a splashing parameter K_c was introduced by Stow and Hadfield (1981) [24], which depends on Ohnesorge and Weber numbers, following eq. (2.4). This relation was validated by other authors, with only slight modifications on the indexes of Oh and We.

$$K_c = We^a Oh^b A \tag{2.4}$$

It is important to emphasize that in most of the following criteria, the droplet velocity (before impact) is only given by its axial component. Mundo et al. (1995) [25], concluded that the impact outcome is strongly affected by the normal momentum, confirming that assumption.

Table 2.2: Transition criteria for single droplet impact, for dry surfaces

Reference	Transition Model	Boundary Conditions and Regimes
Stow and Hadfield (1981) [24]	$K_{cr} = Re^{0.31}We^{0.69}$	Dry surface, depending on surface roughness
Bai et al. (2002) [21]	$We_{cr} = 2630La^{-0.183}$	Dry surface; Adhesion (Stick/Spread) - Splash

2.3.3 Drop Impact onto liquid Films

The previously referred criteria do not consider the liquid film formation at the surface, due to the deposition of droplets, that is observed during spray impact. This deeply impacts the impingement boundary conditions, thus, leading to the modification and higher degree of complexity of the impact mechanisms that trigger the different impact morphologies, as stated in [3].

In this context, an additional parameter called liquid film thickness (δ_f) was defined, which affects droplet impact as is defined as the ratio between the liquid layer thickness (h_f) and the initial droplet diameter (D_0):

$$\delta_f = \frac{h_f}{D_0} \tag{2.5}$$

As referred in [3], this parameter is related with the surface roughness R_a (defined by Randy et al. (2006)). Following this, Tropea and Marengo (1999) divided liquid film impact into four categories:

- Very thin film ($l_r/D_0 < \delta_f < 3{R_D}^{0.16}$): the droplet outcome strongly depends on surface topography (where l_r is the length scale roughness and R_D is the dimensionless roughness $R_D = R_a/D_0$);
- Thin film ($3{R_D}^{0.16} < \delta_f < 1.5$): the droplet outcome becomes less dependent on surface topography;
- Thick film ($1.5 < \delta_f < 4$): the impact only relies on film thickness;
- Deep pool ($\delta_f >> 4$): the impact does not depend on film thickness, nor surface topography.

Despite this categorization, it is not always adopted in liquid film impact studies, since in most cases δ_f is smaller than unity.

Regarding the criteria correlations, they come formulated in terms of K_{cr} in table 2.3. As one can expect, the presence of a liquid film during droplet impact should stimulate the splash effect for a thin liquid film. Mundo et al. (1998) [26] observed that increasing the liquid layer thickness increases the kinetic energy dissipation. Thus, to enter the splashing regime, the droplet must achieve a higher kinetic energy at impact, translating on a higher K_{cr}.

Moreover, Bai and Gosman (2002) [21] did not include the effect of film thickness in their models, instead, they made an analogy between a wetted wall and a dry wall with high roughness, thus assuming very thin liquid layer behaviour.

Table 2.3: Transition criteria for single droplet impact, for wetted surfaces

Reference	Transition Model	Boundary Conditions and Regimes
Mundo et al. (1998)	$K_{cr} = 57.7$	Wetted non-heated surfaces with different surface roughness's
	$K_{cr} = Oh\ Re^{1.25}$	**Complete Deposition – Splash**
Bai et al.(2002)		Wetted surface
	$We_{cr} = 2$	**Stick-Rebound**
	$We_{cr} = 20$	**Rebound-Spread**
	$We_{cr} = 1320 La^{-0.183}$	**Spread-Splash**
Wang et al.(2002)		Wetted non-heated and smooth surface, for $Oh = 0.0316$
	$We_{cr} = 450$	$\delta_f \leq$ **0.1**
	$We_{cr} = 340 + 1375.5\delta_f$	$\mathbf{0.1} \leq \delta_f \leq \mathbf{1}$
	$We_{cr} = 1043.8 + 232.6{\delta_f}^{-1} - 1094.4{\delta_f}^{-2} + 1576{\delta_f}^{-3}$	$\delta_f > \mathbf{1}$

2.4 Droplet Impact onto Heated Targets

Heat transfer effects at a heated surface resulting from spray impingement can be quantified by the correspondent boiling curves. One should notice that surface temperature variation induces complexity to the analysis of the spray impingement phenomenon. An introduction to heat transfer regimes is provided in the following paragraphs.

According to Incropera and DeWitt (2002) [27], the boiling curve represents the variation of heat flux at the surface level according to its excess temperature ΔT_e, which is defined as the difference between surface temperature and the liquid saturation temperature, for a given pressure value. Therefore, four regimes, at different levels of surface superheat, can be identified:

- **Single-phase liquid ($T_w < T_{sat}$):** at lower superheats, heat transfer occurs without phase change by free convection
- **Nucleate boiling ($T_{sat} < T_w < T_{CHF}$):** bubble nucleation starts to be visible close to the wall - (A-B), as bubbles increase their motion, reaching the surface of the liquid film (due to buoyancy forces) - (B-C). This regime is associated with the highest heat transfer coefficients since heat is removed with liquid phase change until it reaches the maximum heat flux, called Critical Heat Flux

CHF;

- **Transition boiling ($T_{CHF} < T_w < T_{Leindenfrost}$):** a vapour layer starts to form, insulating some portions of the surface-liquid interface, while others are still encountering intense bubble nucleation. This results in a reduction of the heat flux, reaching a minimum, at the Leidenfrost temperature;
- **Film boiling ($T_w > T_{Leindenfrost}$):** this regime corresponds to high wall superheats where a stable vapour layer forms, eliminating contact between the liquid film and the surface. This diminishes the heat transfer coefficients, where heat is initially transferred under conduction, and, as the surface temperature increases, radiation starts to play a dominant role in heat transfer.

Following Liang (2017) [1], it is worth noting, that in spray cooling, the optimum cooling for low-temperature applications is achieved by maintaining the temperature range between Onset of Boiling (ONB) and (safely below) CHF, to prevent the reduction in HTC. For higher temperatures, this range is set above Minimum Heat Flux (MIN).

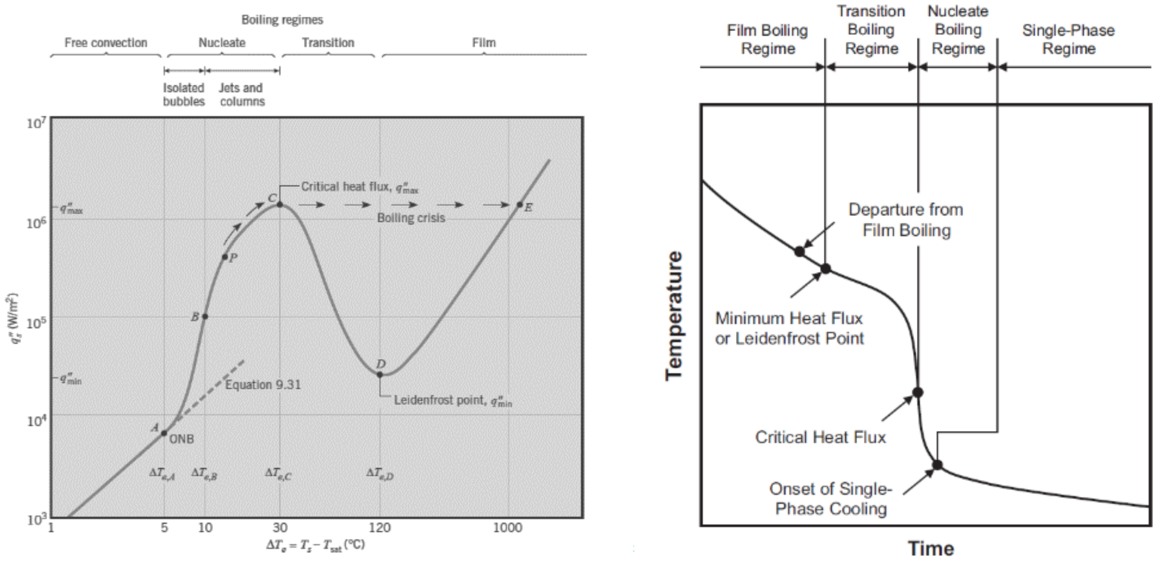

(a) Boiling Curve [27]

(b) Cooling quench curve [1]

Figure 2.6: Typical heat transfer curves

2.5 Spray Impact

It should be noted that most of the referred transition models only consider single droplet impact. A usual simplification assumes the spray as a summation of individual droplets, to use the models presented above. This includes the neglection of the droplet to droplet interaction between different sizes and velocities.

Despite its use, according to [3], these assumptions are quite incorrect, since the interaction between spray droplets are existent and complex.

According to Sielaff (2014) [28], heat exchange at the top of the impinged surface can be deduced assuming an energy balance applied to a pixel, leading to:

$$q'' = q''_0 + k_h \delta \left(\frac{\partial^2 T}{\partial x^2} + \frac{\partial^2 T}{\partial y^2} \right) - \rho_h c_{p,h} \delta \frac{\partial T}{\partial t} \tag{2.6}$$

where q''_0 is the imposed heat flux from the heater (from Joule effect) for the projected area, k_h is the heater thermal conductivity, $c_{p,h}$ is the specific heat capacity of the heater, δ is the foil thickness and q" is the heat flux from the heater to the liquid.

The heated surface (heater) is assumed to have a negligible temperature difference between its upper and bottom side. It is worth mentioning that the energy balance performed by [28] was addressed for a pool boiling situation and was evaluated using a high-speed thermographic camera. Hence, a pixel by pixel calibration was performed by [28] to assure an accurate analysis. A similar approach was performed here, considering, in this case, the liquid film deposited on the heated surface during spray impingement that was already applied to a single droplet impact case on a previous study [29].

2.6 Nanofluid Properties

The introductory chapter of this dissertation has already pointed out some of the thermophysical modifications caused by the addition of nanoparticles on the base fluid. Viscosity, thermal conductivity and convective heat transfer coefficient are fundamental properties in heat transfer [8, 11]. Thereafter, equations regarding their estimation were developed. Most of these equations are derived from classical models, equally used for mixtures of low particle concentrations and low particle diameter, in the range of mili- to the micrometre.

For the thermal conductivity, the classical computation approach will be adopted. Following Maxwell (1891), its estimation considers well-dispersed solid particles on a continuum medium and is given by:

$$K_{nf} = \frac{2K_{bf} + K_p + 2\phi\left(K_p - K_{bf}\right)}{2K_{bf} + K_p - \phi\left(K_p - K_{bf}\right)} K_{bf} \tag{2.7}$$

where ϕ is the volume fraction of the solid particles, K_{bf} and K_p the base fluid and solid particle thermal conductivity, respectively, and considering them as bulk materials.

Later, Hamilton-Crosser (1962), added the effect of particle shape, introducing an empirical shape factor (n) that relates the particle sphericity, resulting in Equation (2.8). From W.H.Qi (2005) [30], the shape factor is the ratio of the surface area of the non-spherical nanoparticle to that of an equivalent spherical nanoparticle with the same volume ($n = S/S^{'}$).

$$K_{nf} = \frac{K_p + (n-1)\,K_{bf} - (n-1)\,\phi\,(K_{bf} - K_p)}{K_p + (n-1)\,K_{bf} + \phi\,(K_{bf} - K_p)} K_{bf} \tag{2.8}$$

Viscosity is another relevant parameter in heat transfer, that largely affects the pressure drop. It depends on the base liquid's viscosity and nanoparticle concentration, as higher particle concentration leads to higher nanofluid viscosity. This property is also influenced by the nanoparticle aggregates which in turn relies on nanoparticle morphology.

The specific heat (c_p) is another fundamental property. It is mainly estimated based on heat equilibrium. According to Xuan and Roetzel (2000), c_p can be estimated as:

$$c_{p_{nf}} = \frac{(1-\phi)\,(\rho c_p)_{bf} + \phi\,(\rho c_p)_p}{(1-\phi)\,\rho_{bf} + \phi \rho_p} \tag{2.9}$$

Finally, the specific mass (ρ), that influences the Reynolds number and pressure drop, can be simply deduced from mass conservation:

$$\rho_{nf} = (1-\phi)\,\rho_{bf} + \phi \rho_p \tag{2.10}$$

3

Experimental Setup, Characterization and Procedure

Contents

3.1 Introduction

The present chapter describes the experimental setup that was used throughout this study. The experimental procedure, as well as data post-processing methodologies and uncertainty analysis, will be also described.

3.2 Experimental Setup

The experimental arrangement used in the present work is schematically represented in Figure 3.1. The fluids under study were atomized and characterized by two distinct system arrangements. The underlined area of the scheme represents the main components of the experimental arrangement that includes the atomizer and the impact surface.

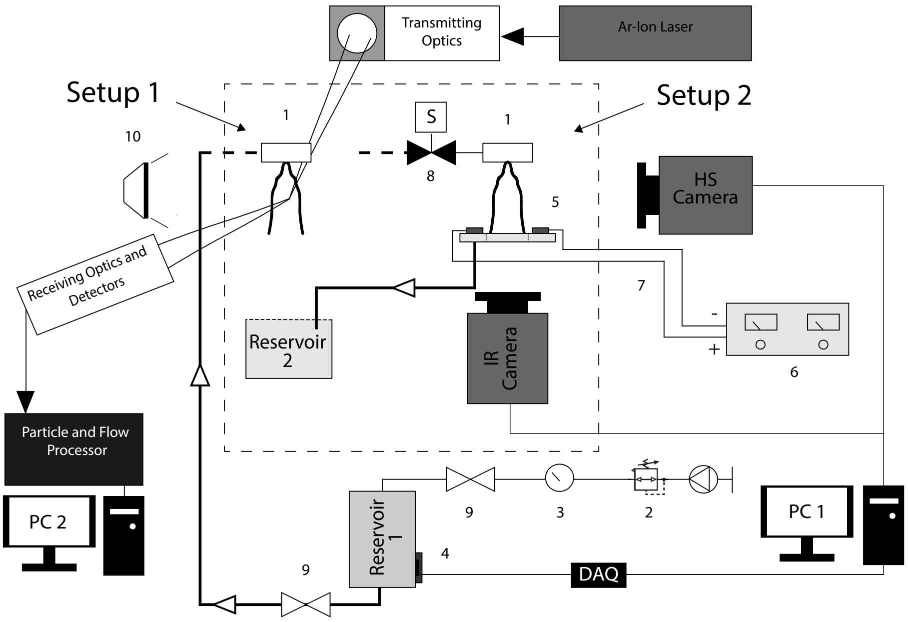

Figure 3.1: Experimental installation scheme: (1) Atomizer; (2) Air pressure regulator; (3) Manometer; (4) Temperature sensor; (5) Impact surface; (6) Power supply; (7) Electric cables; (8) Solenoid valve; (9) Manual valve; (10) Light source

The atomizer (fig. 3.1, index 1) is composed of two parts: the swirl nozzle and the nozzle support that receives the liquid tangentially, they are also represented in Figure 3.2. The swirl nozzle has a discharge orifice of 0.42 mm in diameter and two opposing tangential ports with a squared shaped cross-section of 0.6x0.6 mm^2. Detailed geometrical specifications can be found in [7].

The continuum liquid stream comes from a 3 dm^3 cylindrical reservoir (fig. 3.1, Reservoir 1), that is pressurized by air. The pressurization (relative) was maintained at 87 psi (± 0.5 psi) by a IR1M Monnier

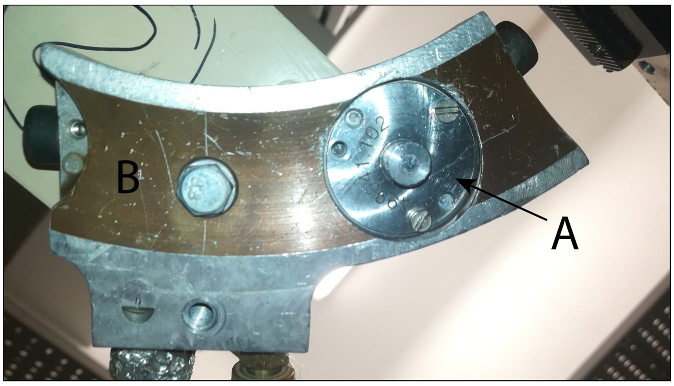

Figure 3.2: Atomizer: (A) swirl nozzle, (B) support

compressed air regulator from Spirax Sarco (fig. 3.1, index 2) and monitored by a manometer (fig. 3.1, index 3).

Additionally, a K-type thermocouple (C03-K from Omega, fig. 3.1, index 4) was mounted on Reservoir 1 and it was connected to a data acquisition board DT9828 from Data Translation (fig. 3.1, DAQ) to measure the liquid's initial temperature.

A PDA system was used to characterize the velocity and size of the droplets that constitute the spray in various points of interest. This system was utilized in Setup 1 and it is composed by a 300mW-400mW Ar-Ion Laser, from Spectra-Physics, a transmitting/receiving optics connected to a particle and flow processor (BSA P80, from Dantec Dynamics).

In Setup 2, the heat exchange between the spray and the heated surface was analyzed. A metallic base (fig. 3.1, index 5) paired with a thin stainless steel (AISI 304) surface was used to characterize the spray impact phenomena. This surface had a thickness of 20 μm and it was heated by Joule effect using a continuous current power supply (HP 6274B DC, fig. 3.1, index 6). Additionally, as this surface was very thin, the temperature variations at its inferior face were captured by a high-speed infrared (IR) thermographic camera (Onca-MwIR-InSb-320, from Xenics). Moreover, a solenoid valve (SV3108 from Omega, fig. 3.1, index 8) was mounted before the nozzle to improve the repeatability of the tests performed with the thermographic camera.

In both setups, a high-speed (HS) camera (Phantom v4.2) was mounted perpendicularly to the spray, allowing not only the capture of the free spray (used in Setup 1) but also the spray impact onto the heated surface (used in Setup 2). Along with this camera, a light source of 50 Watts with a diffusing glass (fig. 3.1, index 10) was mounted on the opposite side of the spray to improve the capture contrast. It is important to emphasize that both (HS and IR) cameras were synchronized for spray impact on Setup 2.

To finalize, after atomization the working fluids were redirected to a reservoir (fig. 3.1, Reservoir 2), where they are filtered and reutilized afterwards. It is worth mentioning that the most relevant thermophysical properties of all the nanofluids used here were evaluated before and after the experimental tests (i.e. before and after atomization). Changes in these properties were observed to be negligible, which supports the argument that there were no significant particle losses in the liquid feeding system or the atomizer, in agreement with a previous study [7].

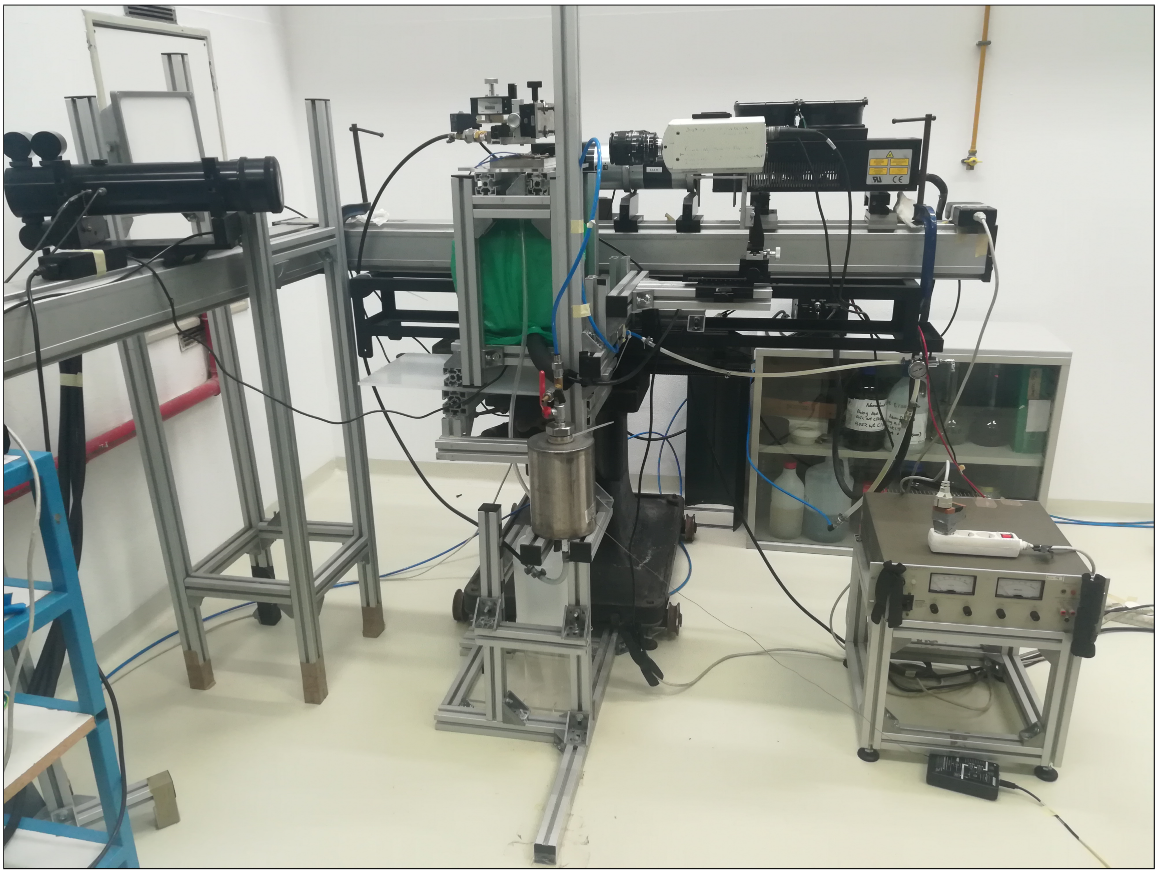

Figure 3.3: Experimental setup

3.3 Preparation and characterization of the nanofluids

One of the key aspects of the preparation of a nanofluid is to guarantee its homogeneity and stability. In this regard, the addition of a surfactant is advised and, in this context, the use of Cetyltrimethylammonium Bromide (CTAB) was adopted. However, one of the downsides of the use of surfactants, including CTAB, is their impact on the liquid's surface tension. Additionally, as different nanoparticle concentrations were going to be used in this study, different surfactant concentrations were required to assure the homogeneity of the nanofluids at higher nanoparticles concentrations. Therefore, the first step was to establish a range of surfactant concentrations and analyze their effect on DI Water surface tension. To that end, different concentrations of DI Water-CTAB mixtures ranging from $0.01 - 1$(wt.%) were prepared and sonicated.

Their surface tension was measured, and their values are represented in Figure 3.4.

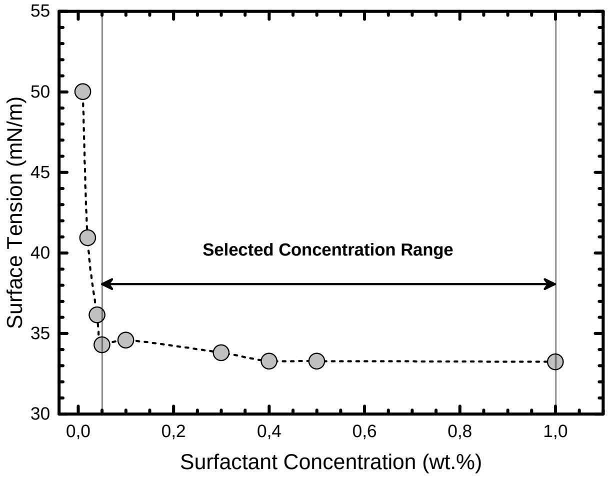

Figure 3.4: Surface tension variation with CTAB concentration in DI Water

From Figure 3.4, a rapid decrease of the surface tension is evident for very low surfactant concentrations (e.g. < 0.04(wt.%)). However, the surface tension value stays constant above 0.04(wt.%), with variations lower than 3.2%. Therefore, the surfactant concentration range was fixed between 0.05–1(wt.%).

Afterwards, the nanofluids were prepared at the Structural Chemistry Center of the Department of Chemical Engineering at IST. These were supplied with different nanoparticle concentrations in the range of 0.1 - 1 (wt.%), mixed with DI Water containing surfactant. Details on their preparation can be found in [31]. Thereafter, these were sonicated using a tip sonicator processor (UP200Ht from Hielscher), for 20 minutes on average at a mean amplitude of 40%. This ensured a good nanofluid homogeneity, as the majority of the nanofluids under study did not show apparent nanoparticle deposition for over a week.

Figure 3.5 represents a sample of the nanofluids under study, after sonication. Initially, they do not show any apparent colour change, nor any deposition at the bottom of the container. Some foam is visible due to the presence of surfactant. After 20 minutes some crystals start to aggregate at the bottom of the fluid number 4, as shown in Figure 3.6. So, to avoid nozzle clogging and fluid instabilities, these were sonicated exactly before use.

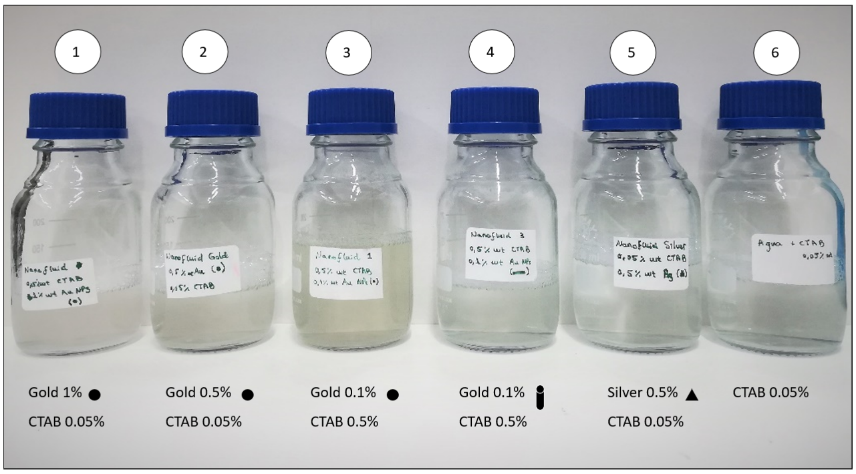

Figure 3.5: Fluids under study, after sonication: (1) Gold Nanospheres 1wt.%, (2) Gold Nanospheres 0.5wt.%, (3) Gold Nanospheres 0.1wt.%, (4) Gold Nanorods 0.1wt.%, (5) Silver Nanotriangles 0.5wt.%, (6) Base Fluid

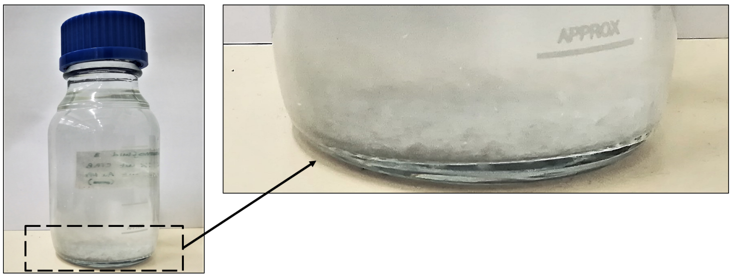

Figure 3.6: Deposition of CTAB crystals in fluid 4.

The main characteristics and thermophysical properties for all the fluids used in this study, measured as described in the following paragraphs, are summarized in Table 3.1.

The thermal conductivity, specific mass and specific heat, were theoretically calculated based on their nanoparticle chemical element and concentration, considering their bulk physical properties (obtained from [32]) and following the Equations (2.7) to (2.10).

Viscosity was measured by the Structural Chemistry Center of the Department of Chemical Engineering, using a rheometer (A instruments ARI 500 ex) at room temperature (20 °C).

Surface tension was measured with an optical tensiometer THETA, from Attension. The pendant drop method was used under controlled room temperatures (20± 3°C). For each solution, 15 measurements were performed and averaged.

The refractive index was also evaluated since it is a fundamental input parameter for the PDA system when considering the 1st order of refraction of a particle [33]. This property was evaluated with an Abbe refractometer (model 60/ED) with a Sodium D1 (yellow) light source at Faculdade de Ciências da Universidade de Lisboa. These measurements were conducted at a controlled temperature (20± 0.1°C), using a thermostatic bath. This procedure was repeated for all the fluids under study following the user's manual instructions. Subsequently, six values of ϕ_s were measured and then averaged. Finally, the sample refractive index N_s was calculated using the following equation:

$$N_s = \sin(\alpha) \times \sqrt{(N_p)^2 - sin^2(\phi_s - \beta)} + \cos(\alpha) \times \sin(\phi_s - \beta) \tag{3.1}$$

where ϕ_s is the scale reading in degrees, $\alpha = 68.000°$, $\beta = 38.000°$ and $N_p =$ 1.76062 , which is the index of the prism glass (at $20°C$), listed in the user's manual for the type of light source used.

3.4 Characterization of the impact surface

The surfaces used for impact were characterized in terms of wettability for all the liquids used. As stated before, the wettability can be quantified by the different equilibrium contact angles (i.e. static angles, quasi-static advancing and receding angles). Even though advancing and receding angles are important parameters in this regard, they were not experimentally obtained due to measuring difficulties and uncertainty, since these working fluids have such low surface tension. Therefore, only the static contact angle was obtained from an average of 5 measurements in 5 different locations of the stainless-steel surface, using an optical tensiometer THETA (from Attension) with the sessile drop method. These measurements are also represented in Table 3.1. Moreover, the surface was considered to be a smooth surface, according to a previous study [34] that used the same surface.

Table 3.1: Thermophysical and Wettability Liquid Properties

Element	DI Water	Base Fluid	Gold				Silver
Geometry	-	-	Spheres			Cylinders	Triangles
Mean Dimensions (nm)	-	-	Diameter: 80			Diameter: 12 Length: 39	Length: 30 Width: 17
Nanoparticle (wt.%)	-	-	0.1	0.5	1	0.1	0.5
Surfactant (wt.%)	-	0.05	0.5	0.05	0.05	0.5	0.05
Dynamic Viscosity µ (cP)	1.002	1.003	1.022	1.038	1.041	1.135	1.038
Specific Mass ρ (Kg/m^3)	998.21	998.71	999.16	1002.94	1007.68	999.16	1002.726
Surface Tension σ (mN/m)	76.34	34.29	33.11	37.75	37.72	32.67	37.30
Specific Heat C_p (KJ/Kg.K)	4.18	4.18*	4.18	4.16	4.14	4.18	4.16
Thermal Conductivity K (W/m.K)	0.6	NA	0.609	0.648	0.6976	0.6094	0.650
Static contact angle (°)	97.55	62.81	53.38	58.10	58.92	51.52	58.77
Spray Cone Angle (°) @87psi	73.64	73.45	73.26	74.40	75.28	73.62	74.97

3.5 Spray Cone Angle Measurements

The HS camera is represented in Figure 3.7, and it was used to record the spray morphology. At this stage, the videos were captured at 13 029 frames/second, with a resolution of 192x192 $pixel^2$ and using an exposure time of 10 μs. A maximum and minimum spatial resolutions of 54.5 μm/pixel and 70.6 μm/pixel were obtained.

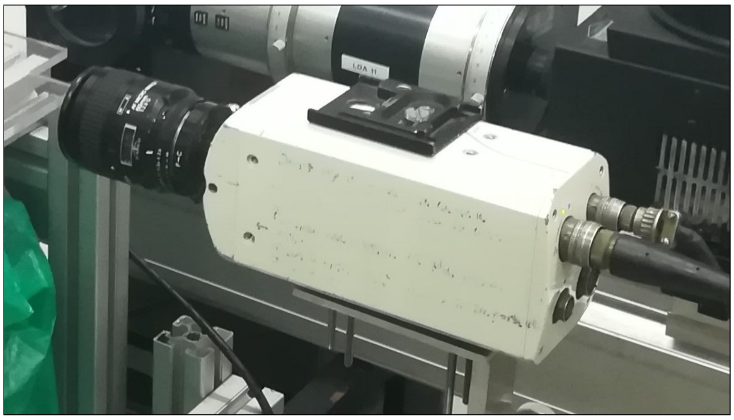

Figure 3.7: Phantom v4.2

The procedure to capture these videos was the following:

- Fill the Reservoir 1 with the working fluid;
- Turn on the air regulator (at the desired pressure) and the light source;
- Capture one initial image with the background and another with a millimetric scale (for the scale capture a time exposure of 74 μs was used);
- Open the Reservoir 1 valve and wait for the spray to stabilize;
- Start the recording and then save it (this was repeated 3 times);
- Close the valve and then leak out the working fluid from the reservoir;
- Clean the reservoir and tubes with DI Water.

After this procedure, the recordings were exported to jpeg images with 8 bits greyscale. Then, these images are processed and analyzed by a MATLAB routine to compute the SCA, in the following order:

1. Enhance the contrast and image clarity (fig. 3.8(a));
2. Subtract the image background to eliminate image defects (fig. 3.8(b));
3. Define the zone of interest by changing the Z_1 and Z_{limit} ;

4. Filter the image by applying a greyscale threshold (typically 200-230), turning the grey scaled image into a binary image (fig. 3.8(c)).

The final step creates the matrix with the left and right coordinates for each Z_i, that will be used as an input on the SCA expression. The fig. 3.8(d)) is just an overlap of the original image with the final.

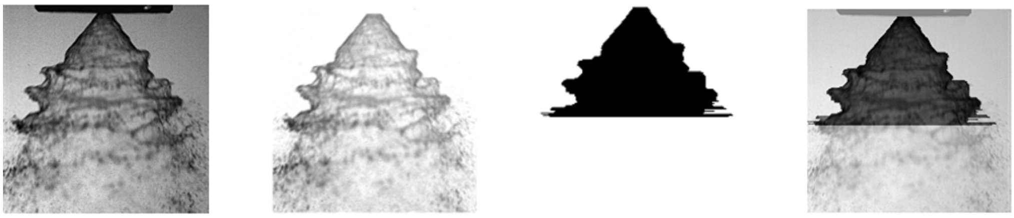

(a) Step 1 **(b)** Step 2 **(c)** Step 3 and 4 **(d)** Comparison with initial image

Figure 3.8: Spray cone angle: image processing steps

Thereafter, with the coordinates of each boundary, the spray cone angle is calculated following Equation (3.2), that is based on triangles similarity:

$$SCA(^\circ) = 2\tan^{-1}\left(\frac{\Delta x_1 - \Delta x_i}{2\Delta Z_i}\right) \tag{3.2}$$

where Δx_1 is the horizontal pixel difference between the left and right boundaries at the 1^{st} pixel of the zone of interest; Δx_i is homologous to Δx_1, but at the i^{th} pixel; ΔZ_i is the vertical difference between the 1^{st} and the i^{th} pixel.

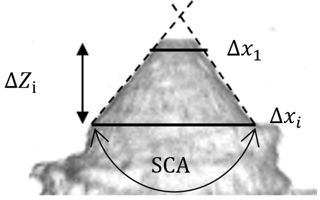

Figure 3.9: Spray cone angle scheme

It should be noted that the zone of interest for the SCA calculation corresponds to the stabilized zone of the spray liquid sheet (before the liquid sheet breakup). In these conditions, 90 different angles are measured for each video frame, where the first angle is measured 10 pixels under Z_1, to decrease the maximum absolute error. After the computation of those angles, the measurements for one video frame are averaged. This process is repeated for the rest of the video frames, that corresponded on average to 1000 frames for each recording. The SCA measurements are represented in Table 3.1, with their respective standard deviations.

Regarding the uncertainties, they were only attributed to the uncertainty of the spray boundaries. Hence, a maximum error associated with their location was defined to be ±2 pixel. Therefore, the associated absolute error can be calculated with the following equation:

$$\delta\alpha = 2\left[\tan^{-1}\left(\frac{\Delta x_i + 2 - \Delta x_1}{2\Delta Z_i}\right) - \tan^{-1}\left(\frac{\Delta x_i - \Delta x_1}{2\Delta Z_i}\right)\right] \tag{3.3}$$

In this regard, the error is maximum at the first computed angle (i.e. at the 10th pixel). From the recordings, a maximum error of 8.43° and a maximum mean error of 2.04° were computed.

3.6 Phase Doppler Anemometer Measurements

The droplet size and velocity distributions were measured using a two-component Phase Doppler Anemometer system. The optical configuration and validation parameters are summarized in Table 3.2. The particle and flow processor P80 was used with the BSA Flow Software v5.10, whose parameters are summarized in Table 3.3. It should be noted that this processor is only capable of performing 1D measurements. Hence, the normal velocity U was evaluated, given its importance for the impact criteria, as discussed in Section 2.3.2.

Table 3.2: Phase Doppler optical configuration and validation parameters

Transmitting optics	
Laser power	300-400 mW
Beam wavelength	514.5 nm
Beam Spacing	60 mm
Transmitter focal length	310 mm
Frequency shift	40 MHz
Receiving optics	
Receiver Type	Classic PDA
Scattering angle	69°
Receiver focal length	500mm
Processor parameters	
Spherical Validation	10%
S/N Validation	-3 dB
Level Validation Ratio	4

It is important to emphasise that the BSA Flow Software user's manual recommends setting the signal gain to 20 dB. However, it was suspected that one of the receiving sensors was malfunctioning. Therefore, to detect the smaller droplets it was initially set at 22 dB, and 26 dB on recent tests.

Table 3.3: BSA Flow v5.10 Parameters

Photomultiplier sensitivity	1180-1500 V
Signal gain	22-26 dB
Center velocity	15 m/s
Velocity span	30-40 m/s
Refractive Index	1.334

The measurements were performed at a distance of 10 mm and 20 mm, which are correlated to the first and second atomization moments [7], from the atomizer. The measured points consist of a radial grid, where $r = 0\ mm$ corresponds to the radial origin of the spray axis. Initially, two sets of measurement grids were adopted: $-20\ mm < r < 20\ mm$ (for Z=20 mm) and $-12\ mm < r < 12\ mm$ (for $Z = 10\ mm$) in 2 mm steps for two perpendicular axes, in order to evaluate spray symmetry and homogeneity, as shown in fig. 3.11.

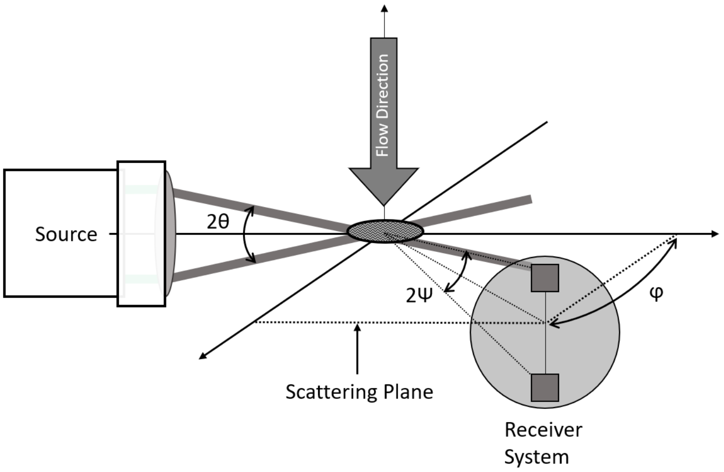

Figure 3.10: Scheme of 3 detector classical PDA set-up, where θ, ψ and ϕ are the beam intersection angle, elevation angle and scattering angle [4]

The number of measured samples, at each point of the grid, was divided into two zones due to the hollow shape of the spray. In this regard, measurements at higher droplet concentration zones were limited to 50 000, to guarantee measurement sample independence, as 35 000 samples are the recommend samples to achieve 2% accuracy for SMD measurements [2]. At lower droplet concentration zones, the number of samples was limited to 5 000. In this case, despite being more sensitive to inaccuracy errors, according to [2], it is considered to be a “reasonably accurate” sample size.

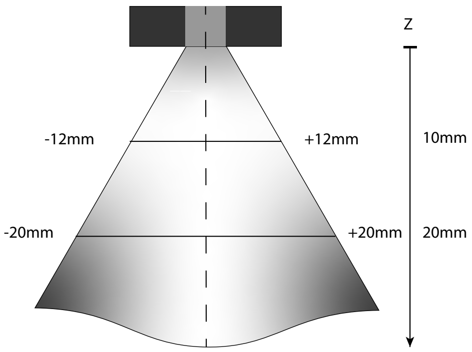

Figure 3.11: Measurement grid used with the phase Doppler system and coordinate system used.

The droplet size and velocity distributions were obtained using a MATLAB routine, that imports data from text files that are exported from the BSA Flow software. Each one of these files corresponds to a radial position, and it contains the measured diameter, axial velocity, the arrival and transit times for each droplet.

Moreover, the referred distributions were characterized by the arithmetic, SMD and the Brouckere mean diameters (D_{10}, D_{32} and D_{43}, respectively). These are defined in [2,33] as:

$$D_{10} = \frac{\sum D_i}{\sum N_i} \tag{3.4}$$

$$D_{32} = \frac{\sum D_i^3}{\sum D_i^2} \tag{3.5}$$

$$D_{43} = \frac{\sum D_i^4}{\sum D_i^3} \tag{3.6}$$

Additionally, the main fractional volume diameters $D_{v0.1}$, $D_{v0.5}$ and $D_{v0.9}$ were obtained, and the Span was calculated and analyzed. Span is characterized as the width or dispersion of the diameter size distribution [9,33], defined as:

$$Span = \frac{D_{v0.9} - D_{v0.1}}{D_{v0.5}} \tag{3.7}$$

3.7 Spray Impact onto the heated surface

The metallic support that holds the heated surface had its dimensions based on the SCA measurements and is represented in Figure 3.12. This support also functioned as a reservoir buffer, as it collects the atomized liquid that falls onto the surface and redirects it to the Reservoir 2.

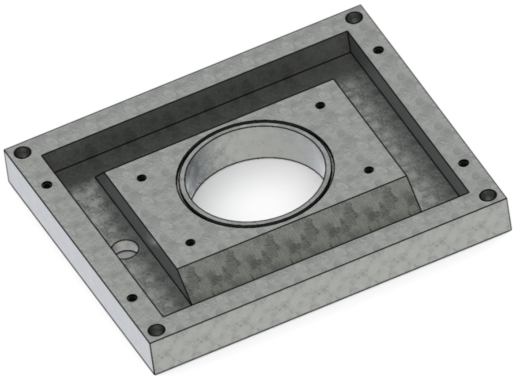

Figure 3.12: Metallic surface support

Regarding the impact surface, it consisted of an AISI 304 stainless steel sheet with a predetermined area of 90x60 mm^2, with a thickness of 20×10^{-6} m. Afterwards, this sheet was fixed to a metallic frame using high-temperature silicone to reduce heat conduction losses and to prevent electrical contact. Thereafter, the bottom side of the surface was painted in black and it was left to dry for 3 hours.

Next, two rectangular copper electrodes were soldered in opposite sides of the sheet, as the surface was heated by Joule effect. It should be noted that this last step involved some issues, majorly due to inexperience when it comes to soldering. As high temperatures were required to solder the two electrodes onto the smooth sheet, some corrugation on its surface forms during cool-down. The solution was to pre-stretch the surface with Kapton tape before soldering as this decreased corrugation. In this regard, the final surface is represented in Figure 3.13.

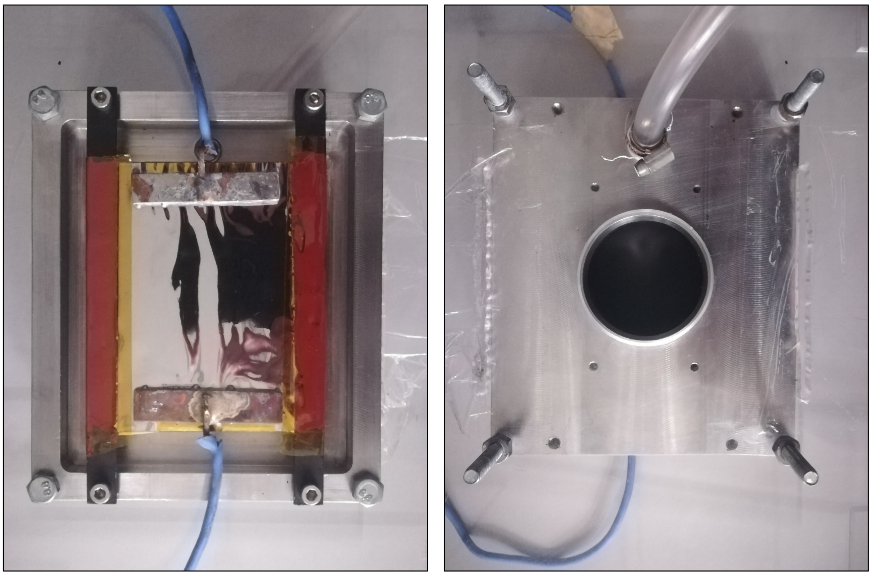

(a) Top view **(b)** Bottom view

Figure 3.13: Metallic support with the final surface

As previously referred, the thermographic IR camera Onca-MwIR-InSb-320 (Xenics), represented in Figure 3.14, was used to depict heat transfer at the surface bottom face. This was painted in black with an emissivity (ϵ) of 0.95, as provided by the manufacturer.

Figure 3.14: Onca-MwIR-InSb-320 (Xenics)

This camera was used with a custom-made calibration curve that was defined in a previous study [29], using an iteration time of 200 μs. In this way, thermographic videos were recorded at 495 frames/second with a resolution of 230x250 $pixel^2$, that resulted in a spatial resolution of 222.22 μm/pixel.

Additionally, the HS camera was used to visualize the spray impact. For these experiments, this camera recorded at 990 frames/second, which corresponds to two times the frame rate of the IR camera recordings, with an exposure time of 10 μs. Its resolution varied from the impact conditions: for $Z =$

20 mm, a 520x320 $pixel^2$ resolution was used, whereas for $Z = 10\ mm$, a resolution of $520x256\ pixel^2$ was adopted. In both cases, a spatial resolution of 64.49 $\mu m/pixel$ was obtained.

3.7.1 Spray Cooling Experiments

Regarding the spray cooling experiments, they were performed at two different impingement heights with two different initial surface temperatures. These temperatures were previously established and correspond to two imposed currents with I= {9A; 15A}, resulting in T_0= {74 ºC; 145 ºC}. The imposed heat flux was calculated following Equation (3.9):

$$q'' = \frac{P}{A_s} \tag{3.8}$$

where q" is the heat flux, P is the power input and A_s is the surface area.

As the surface was heated by Joule effect, the power input can be calculated as:

$$P = RI^2 \tag{3.9}$$

where R is the surface electrical resistance and I is the input amperage.

In this order, the surface resistance can be theoretically calculated as:

$$R = \ \rho' \frac{L}{W \times \delta} = \ 0.057\ \Omega \tag{3.10}$$

where ρ' is the electrical resistivity of the surface (ρ '$= 7.6E \times 10^{-7}\ \Omega/m$), its length $L = 90\ mm$, its thickness $\delta = 20 \times 10^{-6}\ m$ and its width $W = 60\ mm$.

Based on these equations, the imposed amperage of I= {9A; 15A} result in imposed heat fluxes of q''_0= {855 W/m^2 ; 2375 W/m^2}.

Regarding the spray cooling experiments, the procedure was the following:

- Clean the experimental installation with DI water;
- Adjust the spray position and fill the Reservoir 1;
- Turn on the power supply at the desired amperage and wait for the surface temperature to stabilize;
- Start both recordings (HS and IR) and actuate the solenoid valve;
- When the surface temperature is cooled down, stop both recordings and turn off the power supply;
- Clean the surface with pure acetone.

This procedure was repeated at least 3 times for each different condition stated above to guarantee experiment repeatability.

3.7.2 Post Processing of the thermographic recordings

The experimental thermographic data was analyzed using a MATLAB routine developed in a previous study [29]. The recordings from the IR camera were exported in greyscale with 8-bit depth. Each frame of the recordings is converted from Analog-Digital Units (ADU) to temperatures in Celsius, following a calibration curve for an iteration time of 200 μs, referred in [29] .

After this conversion, the images are denoised by subtracting the background frame (1^{st} frame of the recording) and from using the denoise function from MATLAB. Thereafter, the area of interest is defined and the transient variation of the mean temperature and heat flux is computed. It should be noted that the area of interest was always smaller than the total black painted area due to considerable temperature variations on its edges.

3.7.2.A Heat Flux computation

The heat flux computation is based on Equation (2.6). Following [29], a discretization is made to the first and second-order differential terms to each pixel (i), using the upwind method:

$$\frac{\partial^2 T}{\partial x; y^2} = \frac{T_i - 2T_{i-1} + T_{i-2}}{\Delta x; y^2} \tag{3.11}$$

$$\frac{\partial T}{\partial t} = \frac{T_i - T_{i-1}}{\Delta t} \tag{3.12}$$

Replacing these terms in Equation (2.6), the removed heat flux at each pixel is computed. Therefore, the space-averaged heat flux can be calculated by the integration of the heat flux on the selected circular area using the trapezoidal rule (function ”trap”, from MATLAB):

$$\bar{q}'' = \frac{1}{\pi R^2} \int_A q'' dA \tag{3.13}$$

3.7.2.B Wetted Area Computation

The wetted area of the surface was also computed. To compute it, the videos that were already in Celsius and limited to the selected area are loaded (fig. 3.15(a)). Then, the spatial temperature derivative along the horizontal coordinate (x) is calculated (fig. 3.15(b)) for each frame, whose maximum temperature derivative is located, and it should be positioned on the border of the wetted region. After this step, a median filter is applied to the derivative matrix to reduce noise and to prevent isolated maximum derivatives that were outside of the border of the wetted area (fig. 3.15(c)). Thereafter, the threshold temperature is calculated as the average between the temperatures of the maximum temperature derivative and its right neighbour pixel, following the expression:

$$T_{threshold} = \frac{1}{2} \times \left[Temperature(I_1, I_2, t) + Temperature(I_1 + 1, I_2, t)\right] \tag{3.14}$$

where $T_{threshold}$ is the threshold temperature, I_1 and I_2 are the x and y coordinates of the maximum temperature derivative, and t is the corresponding frame.

From that calculation, every pixel with a temperature lower than $T_{threshold}$ is considered to be inside the wetted regime (fig. 3.15(d)). Finally, these pixels are summed and then multiplied by the squared scale factor, and the wetted area is obtained.

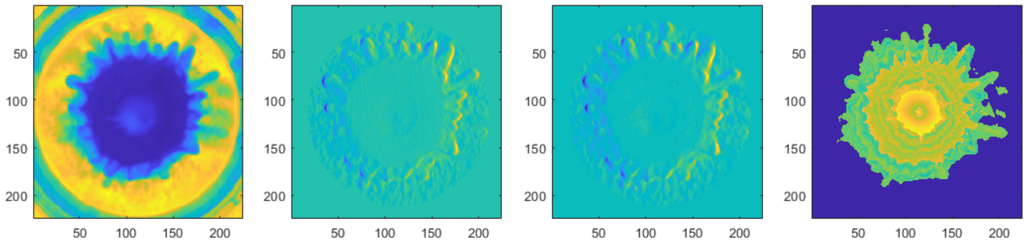

(a) Step 1 **(b)** Step 2 **(c)** Step 3 **(d)** Step 4

Figure 3.15: Wetted Area Computation

Regarding the experimental data uncertainties from the thermographic recordings, these were calculated as:

$$\delta T_{max;min} = \frac{\Delta T_{max;min}}{2^8} \tag{3.15}$$

$$E_{r\ max;min} = \frac{\delta T_i}{T_{min;max}} \tag{3.16}$$

From the tested conditions, the absolute and relative errors were computed and are represented on Table 3.4.

Table 3.4: Surface Temperature Uncertainties from the thermographic experiments

Experiment Conditions	Absolute Error ($^\circ C$)	Relative Error (%)
15 A	0.55	Min= 0.34 Max= 2.70
9 A	0.253	Min=0.30 Max=1.20

4

Experimental Results

Contents

4.1 Effect of nanoparticle concentration on fluid properties

The nanofluids used in this study contain nanoparticles that are composed of different weight concentrations, chemical element and shape. From Table 3.1, it is clear that the nanoparticle addition induces little variations in the thermophysical properties of the resulting nanofluids when compared with the base fluid.

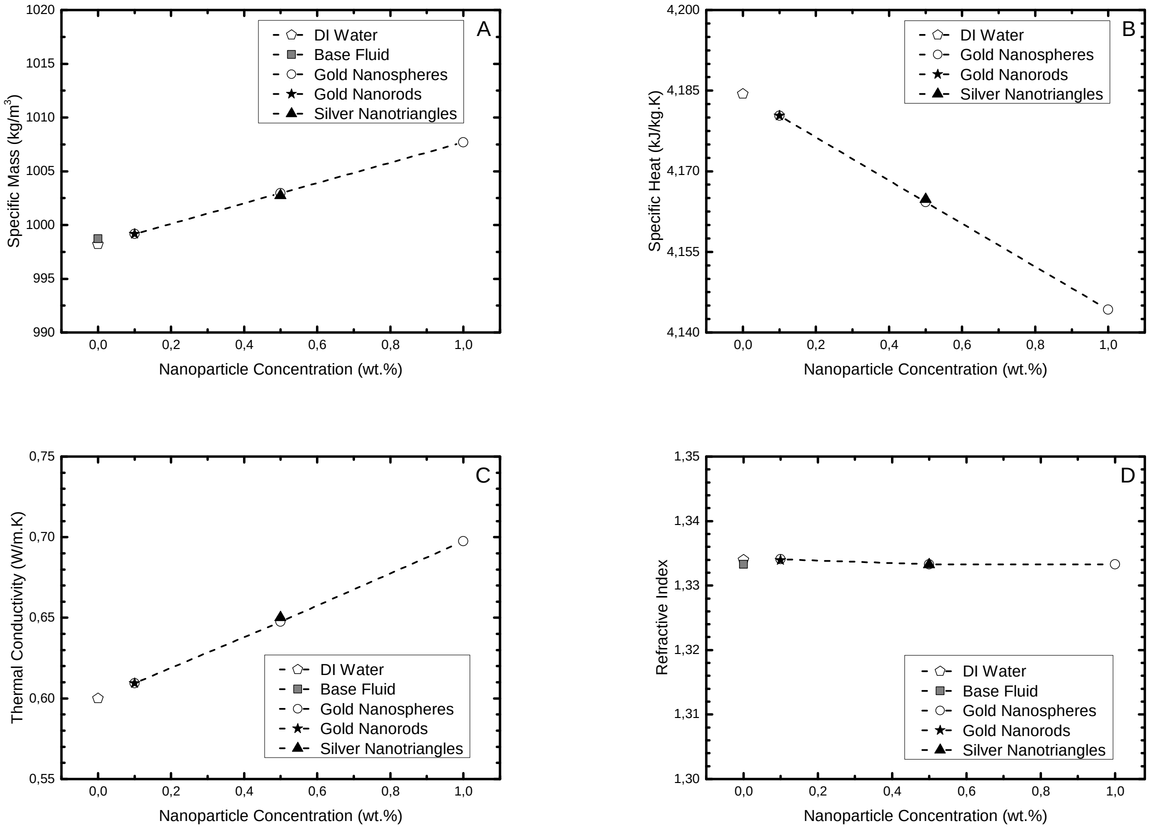

Figure 4.1: Properties variation for the considered nanofluids, at 20°C

Figure 4.1 a) and c) show that higher particle concentration leads, as expected, to an increase in specific mass and thermal conductivity, whereas an opposite trend is observed for the specific heat. The thermal conductivity expresses a major enhancement when compared with DI Water, showing an increase up to 16.3% for the highest gold nanofluid concentration. These observations are in good agreement with [35, 36]. The refractive index value stayed unaffected by nanoparticle addition. This endorsed the use of the water refractive index in the BSA software properties. Although these observations are simple, they show that the nanofluid's thermal conductivity should be higher than that of DI Water.

According to Figure 4.2 (a), the dynamic viscosity increases with the presence of nanoparticles. A linear increase of the viscosity with nanoparticles concentration is observed for the nanofluids with Gold nanospheres. This trend is in agreement within other studies reported in the literature such as (e.g. [11]

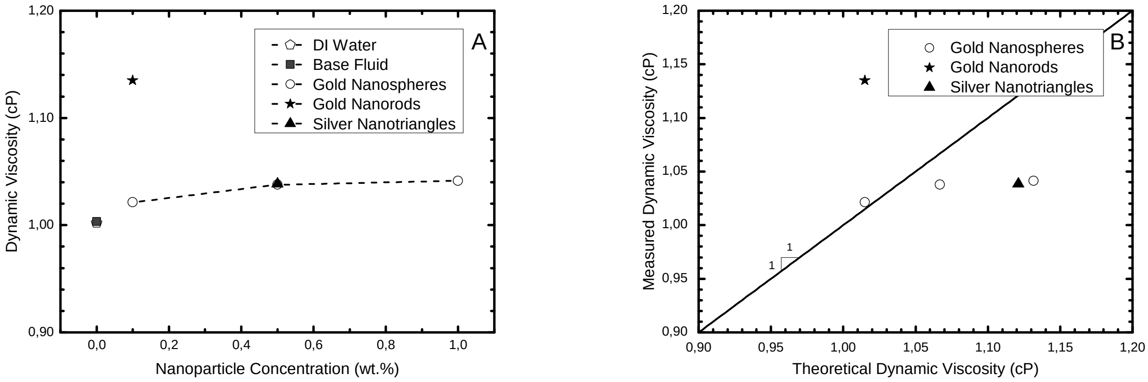

Figure 4.2: Nanofluids viscosity as function of concentration and comparison with Einstein viscosity model

and [36]), as referred in chapter 1. In these studies, the authors suggested that the size and geometry of the nanoparticles play a major role in this regard. When comparing the lowest concentration of Gold nanofluids, one can confirm that the cylindrically shaped nanoparticles, although smaller in size, induce a major increase on the dynamic viscosity when compared with the nanospheres.

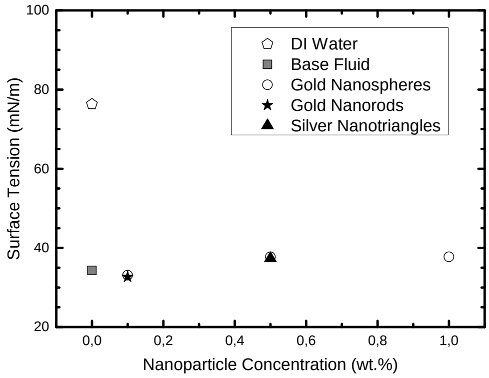

Figure 4.3: Nanofluids experimental surface tension

By analyzing the variation of the surface tension, one can easily detect that the surfactant plays the dominant role in its value, deeply lowering it, as shown in Figure 3.4. From Table 3.1, lower values of surface tension lowers the static contact angle values. Therefore, it enhances the surface wettability, as expected.

Nevertheless, when adding nanoparticles, the surface tension slightly increases when compared to that of the base fluid, as opposed to the observations made in [10]. Moreover, between different nanoparticle materials and concentrations, surface values were hardly modified and show no obvious correlation, as equally observed in [7].

For the SCA, experiments varying the inlet pressures were performed. Figure 4.4(a) shows that its value slightly increases with the inlet pressure, as the liquid film gains tangential velocity. The associated error (95% confidence interval based) is also mensurable and it is related to the natural variation of the

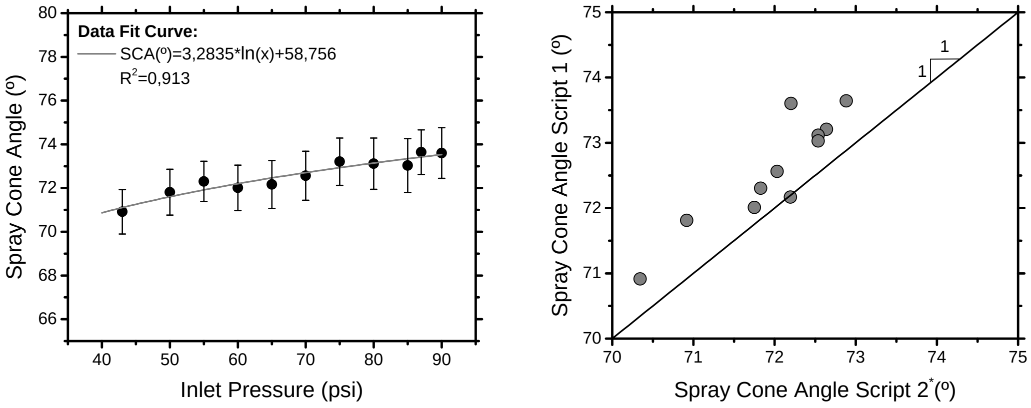

(a) Variation for different inlet pressures

(b) Comparison between script 1, referred in section 3.5, with script 2, from [7]

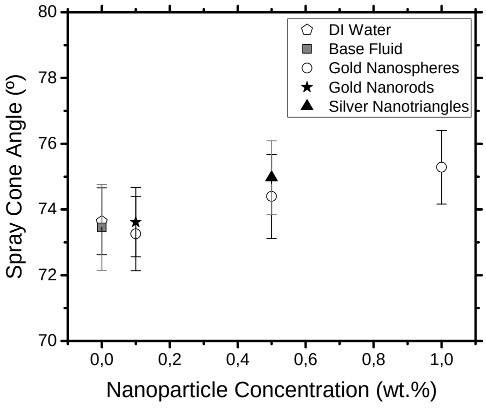

(c) Nanofluid measurements, at 87psi

Figure 4.4: Spray cone angle variation

spray angle. Moreover, as in [2], the value of the SCA should increase with the inlet pressure, until it reaches a limit. This limit is related to the high velocity of the liquid leaving the nozzle, that imposes an increase of the surrounding air velocity, preventing the SCA to increase [2]. However, this SCA limit is not seen in fig. 4.4(a), mainly given to the fact that its computation is made for the stable region of the liquid sheet, that is not so influenced by the induced air currents. In Figure 4.4(b), these results are plotted with the ones obtained from the MATLAB routine used in a previous work [7]. They show a good agreement with each other, with a maximum deviation of 1.9%, which is mainly related to their different distance-to-nozzle measurement location.

From fig. 4.4(c), when adding nanoparticles, no changes outside the margin of uncertainty are observed. However, it should be noted that occasional cloggings were observed probably due to the nanoparticle accumulation inside the nozzle and it reveals that this atomizer is not adequate for nanoparticle use.

4.2 Spray dynamics and morphology (before impact)

4.2.1 Droplet Size and Velocity Analysis using DI Water

The atomization process is characterized by a sum of stochastic phenomena, generating a wide range of droplets sizes with different velocities. The best way to accurately represent these distributions is by showing them in histograms [2, 9]. However, not all the distributions will be shown, as it would be quite exhaustive. Therefore, a simpler approach will be conducted, as they will be represented by their mean values. The mean droplet diameter (D_{10}) was adopted in this case.

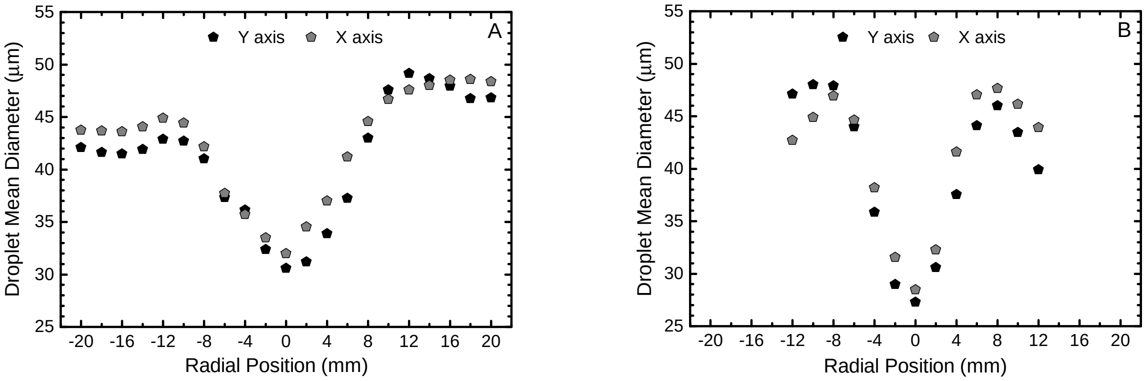

Figure 4.5: D_{10} variation across several radial positions for Z=20 mm (A) and Z=10 mm (B)

Regarding the experimental data, acceptable spray repeatability and droplet mean diameter (D_{10}) symmetry, in both perpendicular axes (x and y,) was verified, as seen in Figure 4.5. Nevertheless, Figure 4.5 reveals a decreased value of D_{10} at negative radial positions than that for positive positions. This is attributed to the relative position of the measuring volume. Therefore, for positive radial positions, the laser beams pass through the cone region of the spray which has a high droplets density, which in turn lowers the validation rate and the detection sensitivity of smaller droplets. This behaviour was also present and explained in a previous study [37].

As the spray under study represented overall good symmetry and axis independence, the measurement grid was reduced to the positive radial positions in only one axis (x, in this case). In this order, Figure 4.6(a) and Figure 4.6(b) represent the droplet mean diameter (D_{10}) and the mean axial velocity (U) for both Z= {10; 20} mm. Additionally, Figure 4.7 shows the histograms at three different dimensionless radial positions r*={0; 0.5; 1}, where $r^* = r_i/r_{max\ Z_i}$, at each vertical distance from the nozzle (Z).

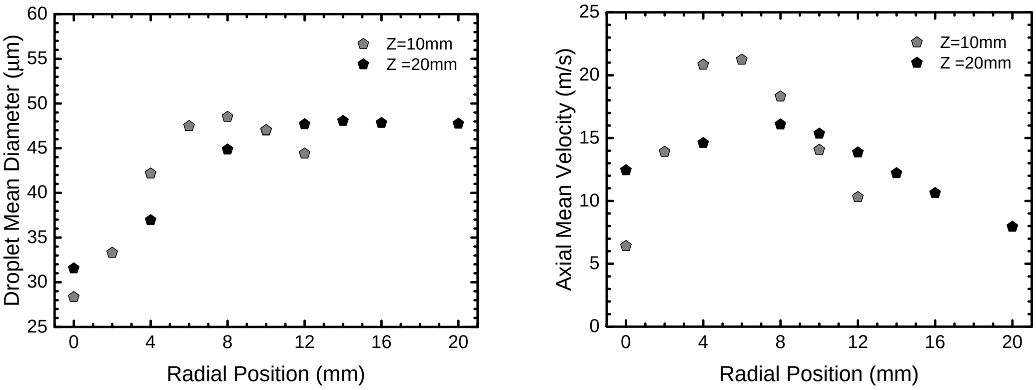

(a) Droplet Mean Diameter Distribution **(b)** Axial Mean Velocity Distribution

Figure 4.6: Mean values for DI Water at Z= {10; 20} mm

At Z=10 mm, the smallest and slowest droplets are found at the centre of the spray (r= 0 mm). This is related to the spray swirling motion and its hollow pattern. Therefore, these droplets are transported to the centre due to the swirling motion, as they have a lower mass. Moreover, increasing the radial measuring distance, the droplet diameter and velocity increases until they reach a maximum around (6 mm $<$ r $<$ 8 mm). At this interval, the atomization intensifies as the droplet rate also reaches its maximum. For r $>$ 8mm, the D_{10} slightly decreases, however, the axial velocity sharply decreases. This happens because, as the measuring zone is reaching the exterior of the spray, the droplets begin to interact with the surrounding air mass that is at a much slower velocity.

Increasing the vertical distance from the nozzle (Z) to 20 mm, a similar D_{10} behaviour is observable. At the centre, the smallest D_{10} is found and its value increases until r= 12 mm. Regarding the axial velocity, it also maintains the same behaviour when it comes to its mean values. However, observing the velocity histograms at r*=0.5 and r*=1 (histograms N and O) a bi-modal distribution is noted, in Figure 4.7. These additional nodes around lower velocities are attributed to the formation of a vortex structure at the edges of the tube which recovers the fluid, creating this wall effect, as it re-atomizes low mass droplets (as seen in on the left sides of Figure 4.7 Q and R) that are transported by this moving air mass.

Finally, it should be noted that the diameter histograms display a log-normal distribution in every position.

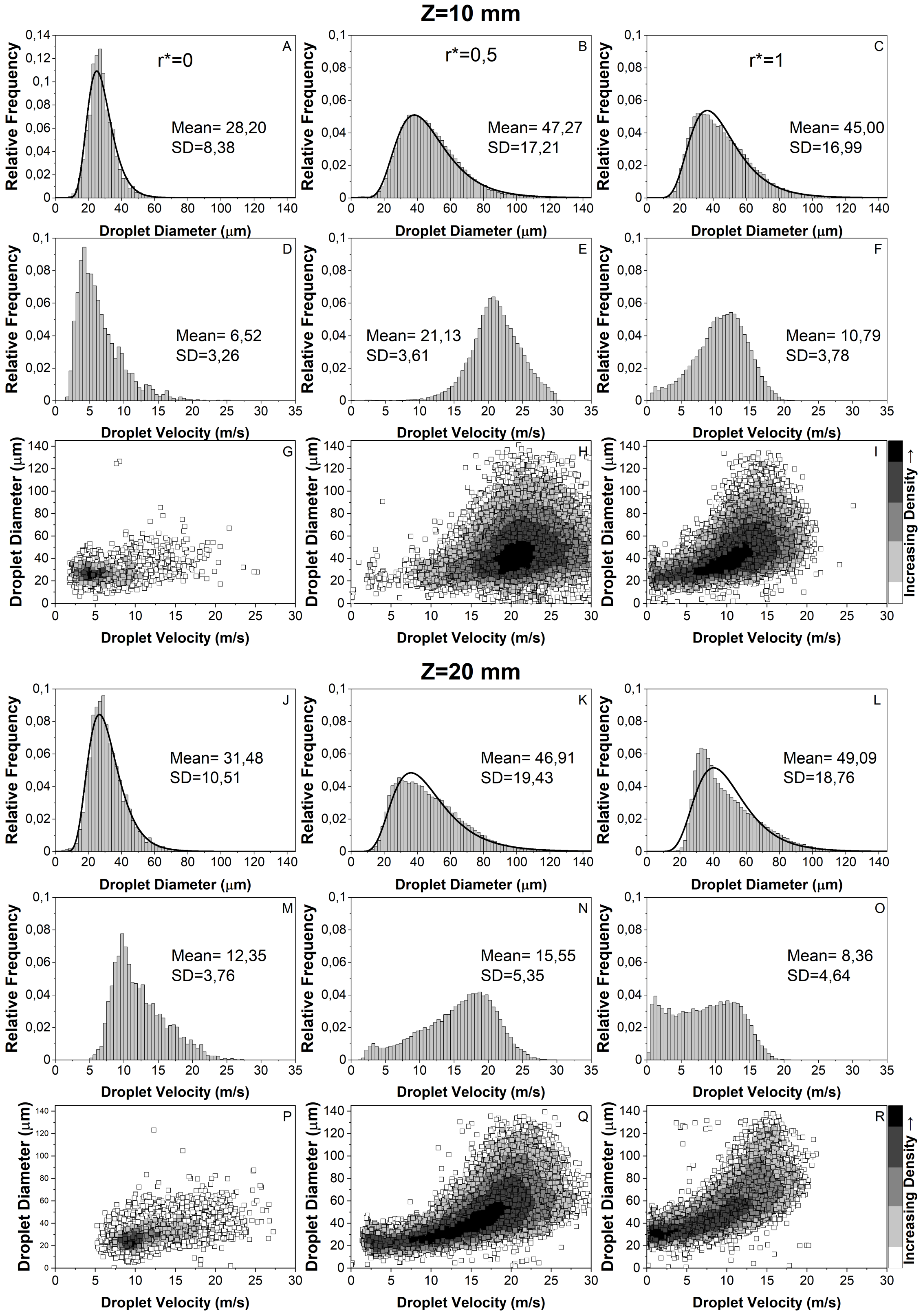

Figure 4.7: Droplet size and velocity histograms and scatter plots for r*= {0; 0.5; 1}

4.2.2 Effects of surface tension and nanoparticle addition

Figure 4.9, graphs A and B, represent the D_{10} measurements across the radial distance, for the different axial distances from the nozzle, Z=10 mm and Z=20 mm, respectively. A decrease of its value is evident for liquids with lower surface tension when compared with DI Water. This behaviour, that lowers the mean droplet mass, combined with the decrease of the axial velocity (U) decreased the Reynolds number (see Figure 4.9, graphs G and H). Opposed to the Reynolds number, the Weber number increased for lower surface tension liquids (see Figure 4.9, graphs I and J).

These observations reinforce that the surface tension plays a major role in atomization (for the same viscosity value) promoting the liquid sheet breakup. This also increases the formation of droplets, as shown in Figure 4.8, without altering the validation rate of the PDA measurements.

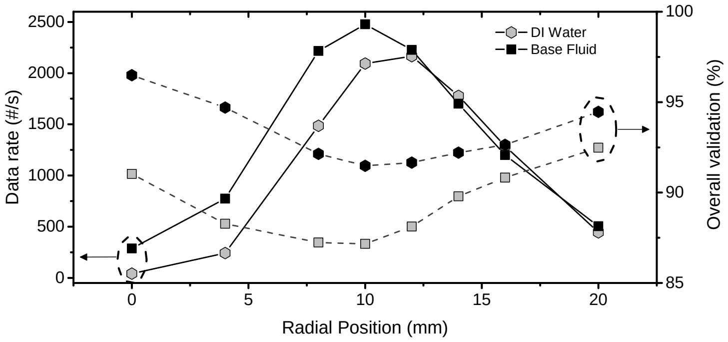

Figure 4.8: Data rate and mean droplet validation for the considered liquids, at Z=20mm

The addition of nanoparticles to the base fluid does not change the values of diameter/velocity, with only a few exceptions (e.g. silver nanotriangles and gold nanorods). Still, these exceptions could be attributed to experimental error (for Z=10 mm). However, for Z=20 mm, these values were mainly affected by increasing the signal gain from 22 dB to 26 dB for these two fluids, due to problems with the PDA receiving probe, decreasing the overall validation rate.

Yet, the addition of nanoparticles seems to increase the relative span (Figure 4.9 C and D) around the central coordinates ($r \leq 2mm$), for some fluids, increasing the dispersion of the diameter size distribution. However, at different Z, these Span values around the central coordinates have no relation with nanoparticle chemical material, nor concentration. Having this in mind, and the fact that the central measurements have lower sample size (5000 samples against 50 000), any spray instability, like a mild clogging, could cause these Span differences.

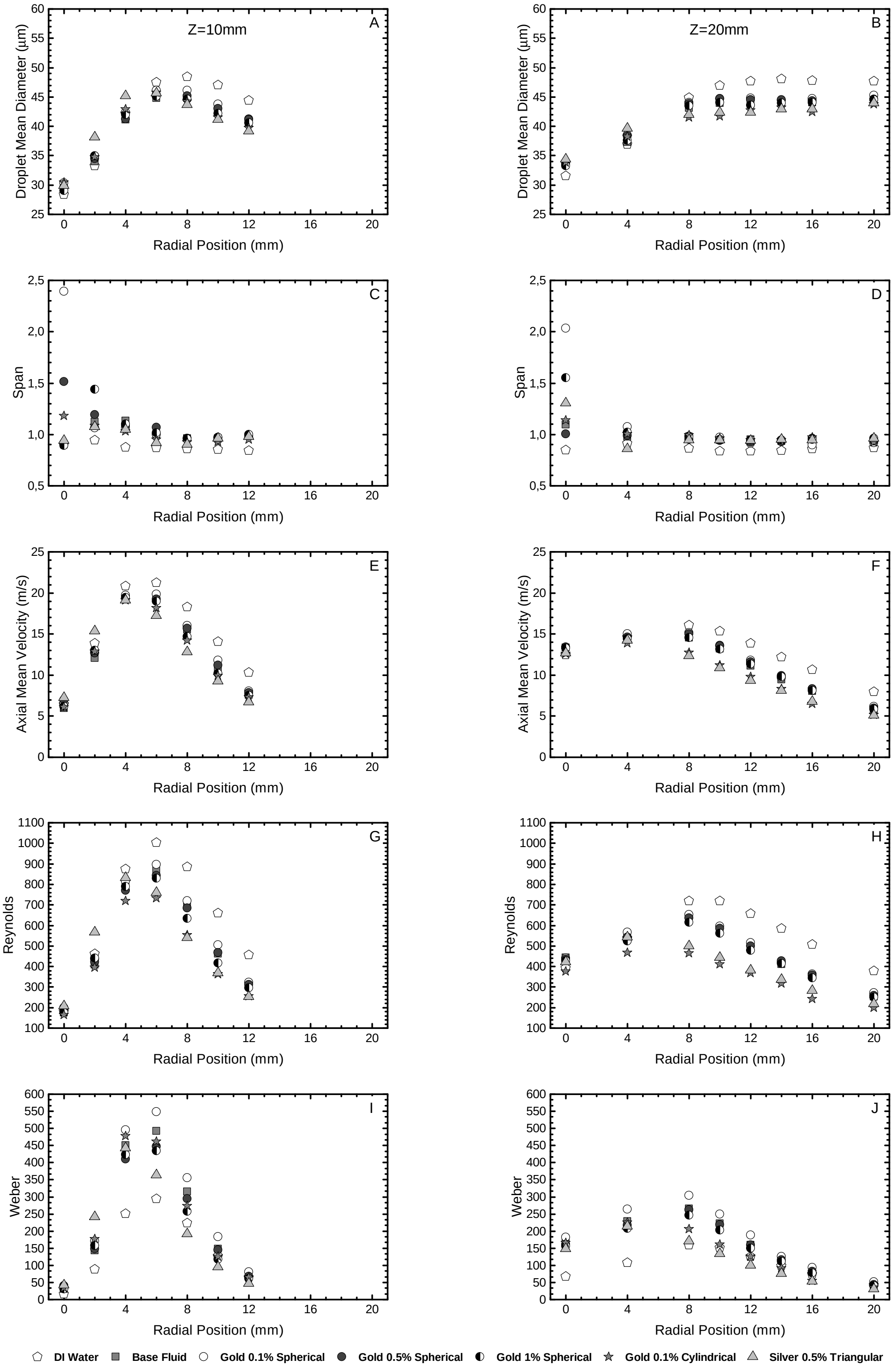

Figure 4.9: Droplet mean characteristics measured with the PDA at different radial positions: A,B - Droplet mean diameter; C,D - Span, E,F - Axial mean velocity, G,H - Mean Reynolds number and I,J - Mean Weber number. Left column corresponds to measurements taken at Z=10mm, while the right column corresponds to the measurements taken at Z=20mm.

4.2.3 Spray Impact Predictions from PDA Data

From the previous subsection, the addition of surfactant slightly decreased the Reynolds number and increased the Weber number. These opposing behaviours will increase the Ohnersorge (Oh) number at those measuring locations. Therefore, one should expect higher values of the Ohnesorge number for slightly lower values of the Reynolds number. In this order, this should induce a vertical displacement of the Oh-Re distribution for those fluids relative to DI Water. Hence, the outcome of droplet impact should slightly change, as will be discussed in the following paragraphs.

Figure 4.10 represents the different threshold criteria for the occurrence of the various droplet impact outcomes according to Bai et al. (2002), referred in Table 2.3, for a wetted surface for $Z = 10\ mm$ and $Z = 20\ mm$. At the centerline of the spray (r*=0), differences between $Z = 10\ mm$ and $Z = 20\ mm$ are visible (Figure 4.10, graphs A and B). At 10 mm, the spread is the predominant outcome, whereas, at 20 mm, the loss in normal momentum extends the droplet outcomes to the stick region.

At r*=0.5 (Figure 4.10, graphs C and D), both splash and spread are the dominant mechanisms and linked with high axial velocities and higher droplet diameters (see fig. 4.9). An additional factor is that these droplets hypothetically collide with the surface at an angle and promotes the formation of secondary droplets, but this subject will not be discussed in this dissertation.

Moving to the spray edges (r*=1), the bi-modal flow that is also dominated by low-velocity droplets, transported by the vortex structure formed at the wall, induces the stick dominance at both heights.

It is important to emphasize that these criteria were developed to estimate the droplet impact outcome on a wall. In this case, the data was collected from a free spray structure that would differ from another with wall impingement, and they overestimate the occurrence of the spreading mechanism, as outlined in [37,38].

Regarding the effect of adding the nanoparticles, there are no observable changes when it comes to the impingement outcome within the range of concentrations considered here, even considering the difference in their physical properties. Again, this is a good indicator that spray dynamics are unaffected by their presence in the base liquid.

To summarize, the majority of the impinging droplets are outside of the splash regime. Therefore, they will contribute to heat flux removal from the surface, and the presence of nanoparticles does not significantly shift the impact outcomes to the splash regime.

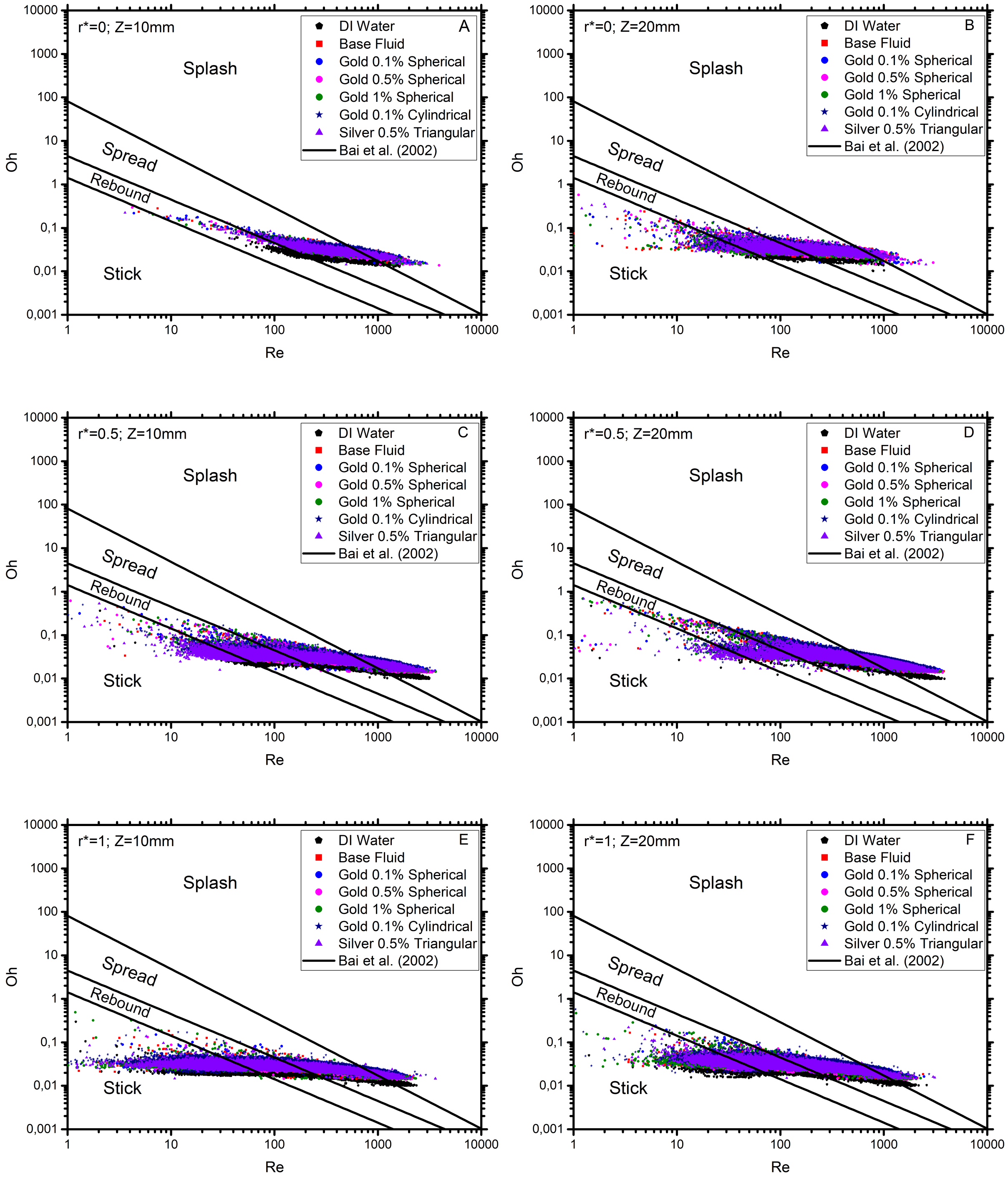

Figure 4.10: Impact outcome prediction for the considered fluids

4.3 Heat transfer analysis (during impact)

4.3.1 Introduction

The first part of this study aimed at the determination of evident changes on the spray morphology and dynamics, and the presence of nanoparticles did not significantly its morphology. For this second part of the analysis, the heat transfer of sprays with nanofluids will be investigated and compared with the base fluid and with DI Water.

As before, two different impact distances (Z=10mm and 20mm) and imposed heat fluxes where used in this study section. Initial temperatures under ($74^\circ C$) and above ($145^\circ C$) the saturation temperature were analyzed. Each combination was repeated at least three times to guarantee experimental repeatability, as shown in Figure 4.11. Overall, the experiments showed good repeatability for all the fluids in the study. Hence, the results represented in this section are shown for one isolated experiment to guarantee a good match of the temperature and heat flux transient variation with their correspondent IR and HS images.

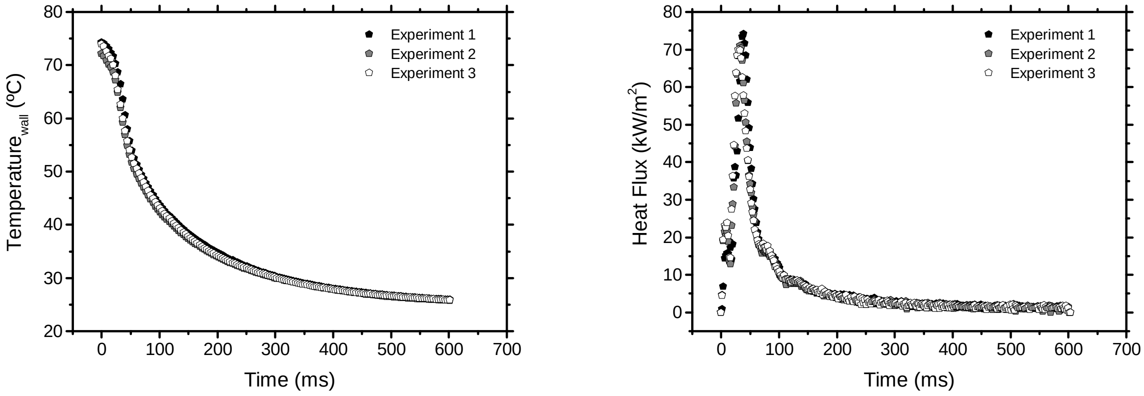

Figure 4.11: Cooling experiments repeatability using DI Water (I=9A, Z=10mm)

Before comparing the different nanofluids heat transfer, an analysis regarding the different changes in the conditions was performed, using DI Water. Primarily, the interest time instances are presented, considering the HS and IR images, the temperature and heat flux distributions.

4.3.2 Spray thermal analysis

Figure 4.12 represents relevant captured instances during wall impact using the IR camera and HS camera. IR images also show the temperature distribution across the radius, with an impact distance of 10 mm and an initial surface temperature of $145^\circ C$.

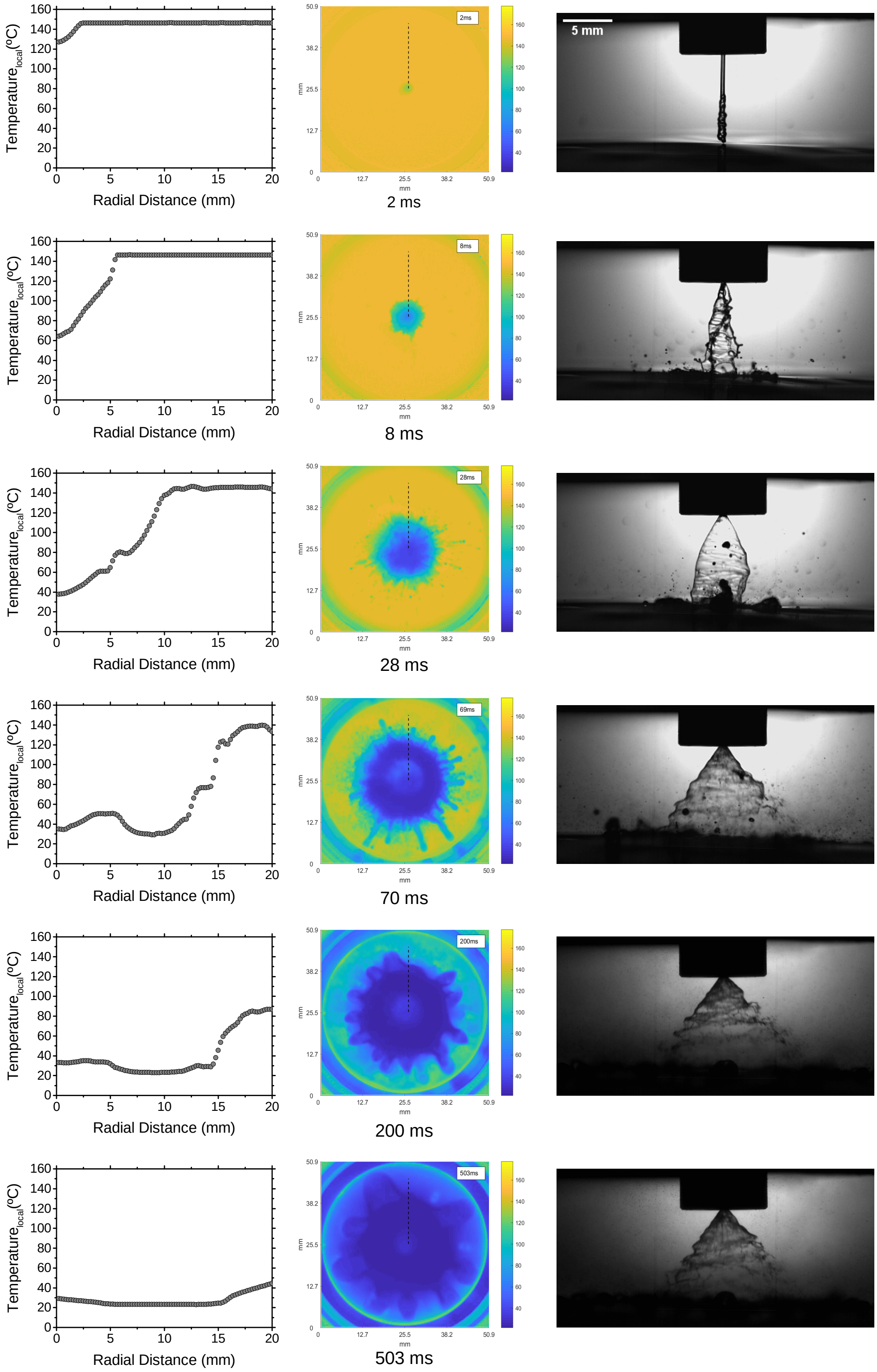

Figure 4.12: a)Temperature variation along the radial profile (identified in the IR images by the black dashed line) during spray impact on the heated surface, b) IR images taken from the backside of the surface, synchronized with c) Side views (taken with the high-speed camera) of the spray showing its dynamics for DI Water. (q”=2375W/m^2, $Z = 10mm$)

The frame before liquid contact sets t_0, where the initial temperature is at a constant temperature. At 2ms, the initial contact is made, and the spray is just a thin liquid structure, far from developed, as seen previously. According to [2], this stage is designated as “thin distorted pencil”. At t=8ms, although roughly visible, the spray starts to form a hollow liquid sheet and some disruptive ligaments start to be visible. Hence, the formation of the first droplets, due to liquid sheet breakup and due to impact, start to arise.

At 28ms, an almost closed hollow smooth liquid sheet, contracted by surface tension forces, is formed. One can qualitatively say that the droplets, resulting from splash or primary atomization, become smaller.

As the velocities increase, at 34ms, the surface tension forces do not hold the closed bubble, as it starts to straight the cone, becoming almost developed. Also, at this point, a major part of the analyzed surface area is wetted by the impacting liquid, forming a liquid film, due to deposition. Hence, the overall removed heat fluxes become maximum, as shown in fig. 4.13, as the active cooling area or film liquid line front becomes higher.

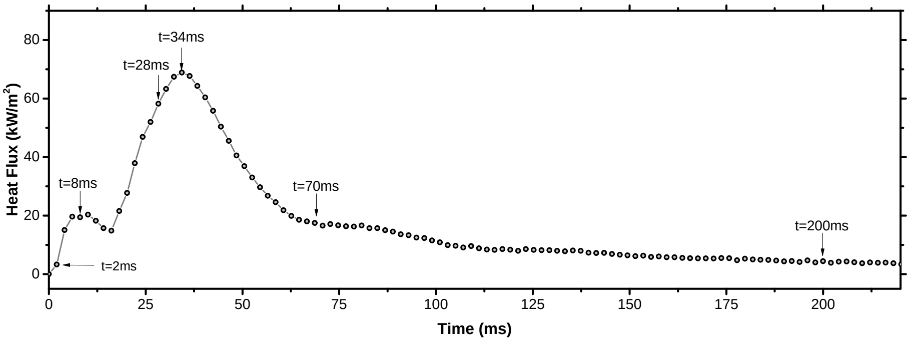

Figure 4.13: Space Averaged Heat Flux (I=15A, Z=10mm)

At later time intervals ($t > 70ms$), as the temperatures and heat fluxes start to stabilize, the formation of secondary droplets at the edges of the spray becomes more intense. This phenomenon results from droplet splash onto the liquid film. In theory, the spray cooling efficiency should decrease, since the number of droplets leaving the surface without promoting heat transfer becomes higher. However, the measurements performed here cannot evaluate this mechanism with the required accuracy to confirm this trend.

Figure 4.14 also shows the mean local temperatures and heat flux for three experiments with identical conditions, where the dark area corresponds to the data dispersion. One can state that the initial and final instances show a lower margin of error, being less sensitive to spray randomness, contrary to $28ms < t < 200ms$.

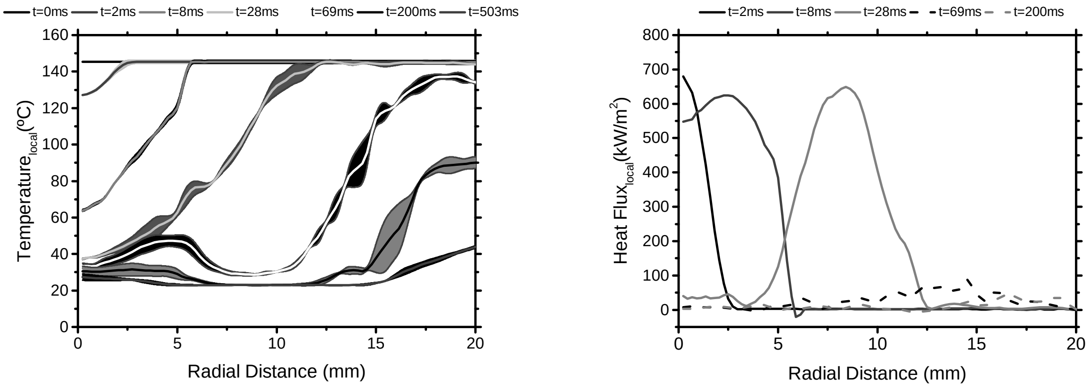

Figure 4.14: Local temperatures and heat fluxes at different time instances (I=15A, Z=10mm). The shadowed area corresponds to the dispersion of the points

4.3.3 Effect of the surface temperature in the removed heat flux

The cooling transient curves for two different imposed heat fluxes are shown in Figure 4.15, for $q''_{imp} = 2375\ W/m^2$ and $q''_{imp} =\ 855\ W/m^2$, resulting in initial temperatures of $145°C$ and $74°C$, respectively. An increase of the initial surface temperature increases the removed heat flux, as expected. The main reason is given to the increased temperature difference ΔT between the surface and liquid. Furthermore, the transient cooling heat flux curve reveals a local maximum before reaching the absolute maximum, as referred before.

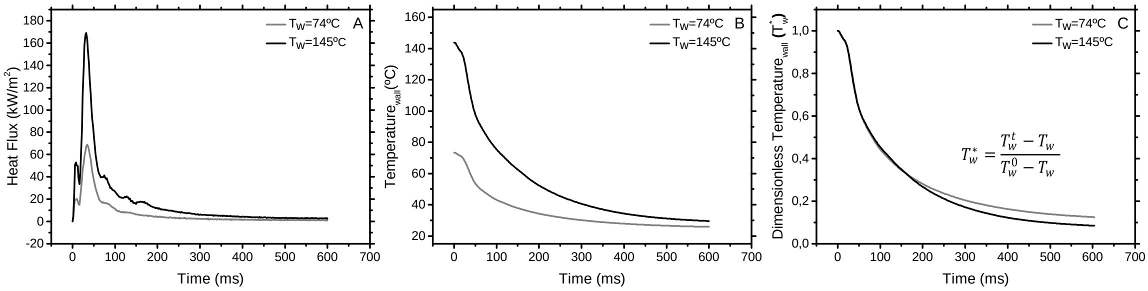

Figure 4.15: Temporal variation of the: a) wall removed heat flux; b) wall temperature; c) dimensionless wall temperature for DI Water (Z=10mm)

For both initial temperatures, the formation of a liquid film layer is present, and the formation of bubbles due to the formation of vapour were not observed. This can be justified either by the fast-dynamic impact, that prevents these observations, or most probably the imposed heat flux was not high enough. Moreover, this also reveals that the initial temperatures are below the temperature of critical heat flux. Figure 4.15 (c), besides showing a higher decay of the dimensionless temperature for $T_w = 145°C$, the temperature variation showed the same profile.

4.3.4 Effect of impingement distance

Higher impingement distances result in higher averaged heat fluxes, promoting the temperature decrease rate (Figure 4.16). This observation can be explained by the increase of the wetted cooling area, that increases with impingement distance due to the SCA, causing the droplets to disperse in a bigger area. This behaviour is explicit in Figure 4.17, where the estimated cooling area is plotted for two distances. The cooling area for Z=20mm is always higher than for Z=10mm, with a maximum experimental variety of 10.52%. Additionally, a maximum cooling area difference of 4 cm^2 is given at 57 ms and it corresponds to 65.5% of the cooling area for Z=10mm. Moreover, it is important to note that the droplet impingement area was smaller than the black painted area.

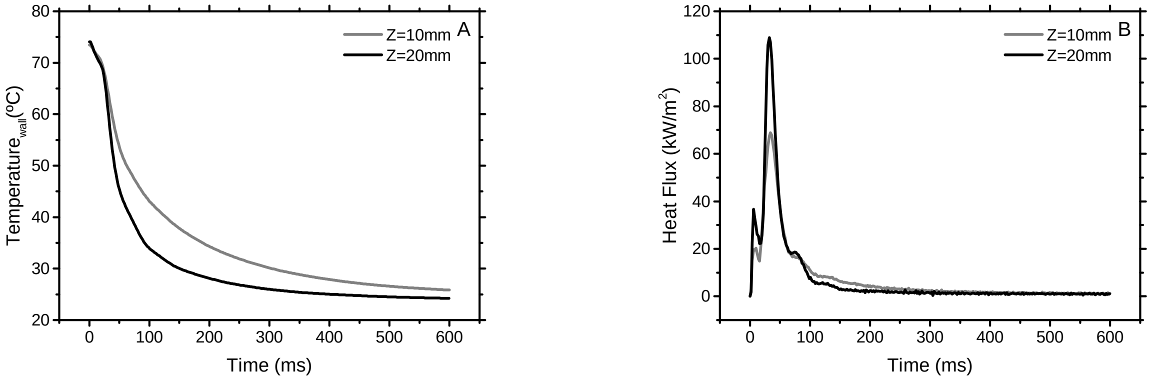

Figure 4.16: Temporal variation of the wall: (A) space averaged temperature; (B) removed space averaged heat flux for DI Water

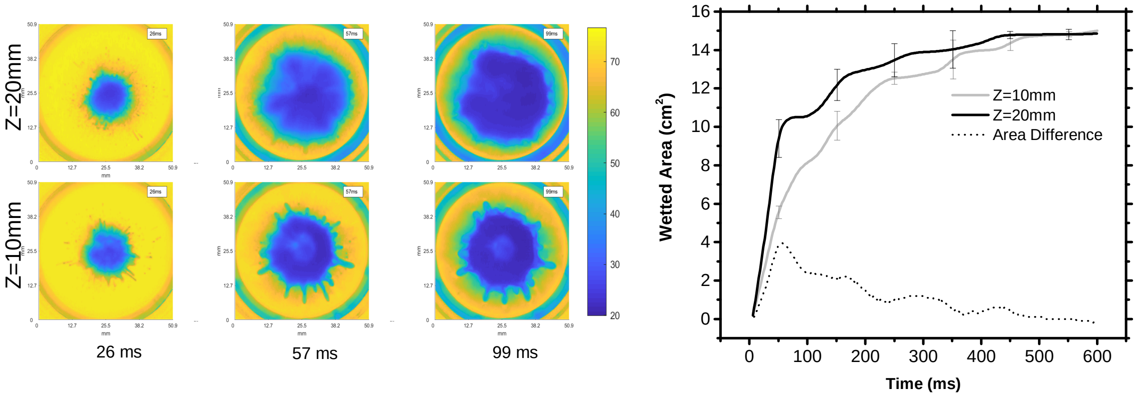

Figure 4.17: IR frame comparison (left) and computed wetted area (right) at two different impact distances for DI Water with $T_0 = 74°C$

4.3.5 Effect of surface tension

The nanofluids used in this study were mixed with a surfactant to improve their stability. However, the presence of surfactant reduces surface tension. Therefore, an analysis of its effects was performed, using the same conditions ($Z = 20\ mm$ and $T_0 = 145°C$).

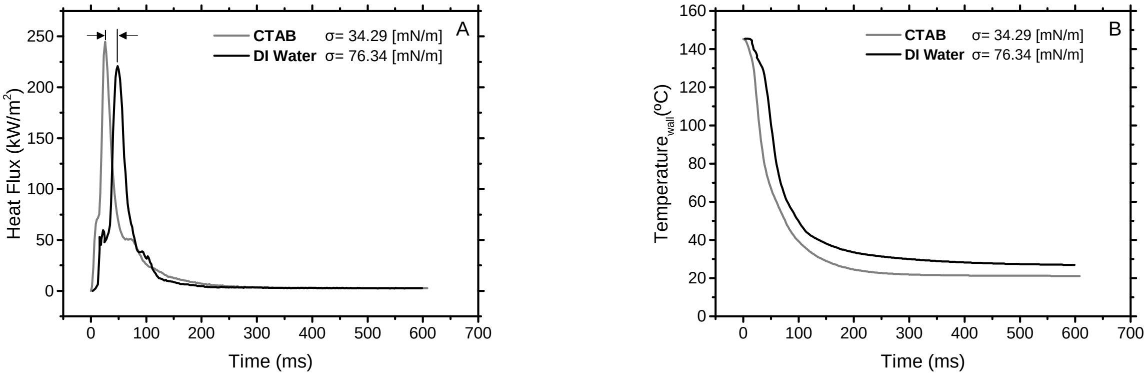

Figure 4.18: Effect of surface tension on: (A) Space averaged heat flux and (B) Space averaged temperature (T_0=145$°C$, Z=20mm)

From Section 4.3.5, the maximum heat flux occurs at a lower time interval with the presence of surfactant. From Table 3.1, the decrease of the surface tension decreases the contact angles. This should enhance heat removal, as the droplets impacting the surface would spread more easily, hence covering a bigger area for the same liquid volume, as indicated in Figure 4.19.

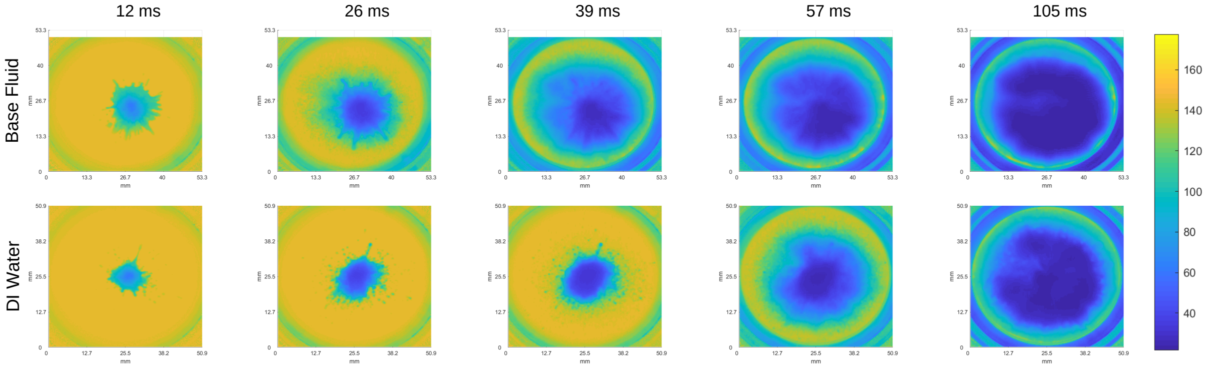

Figure 4.19: IR images at different time steps showing the effect of the decreased surface tension between two liquids

Furthermore, the cooling area differences between the two fluids are evident from 26 - 57 ms in Figure 4.19. From Figure 4.20, the wetted area of the Base Fluid is always higher than that of the DI Water, inside a margin of 16.5%, whose maximum difference is mainly given at 39 ms. Therefore, the cooling area of the base fluid increased due to its lower surface tension, promoting the earlier generation of droplets which in turn enhances the spray radial expansion in time. This is consistent with the increased data rates measured in Figure 4.8.

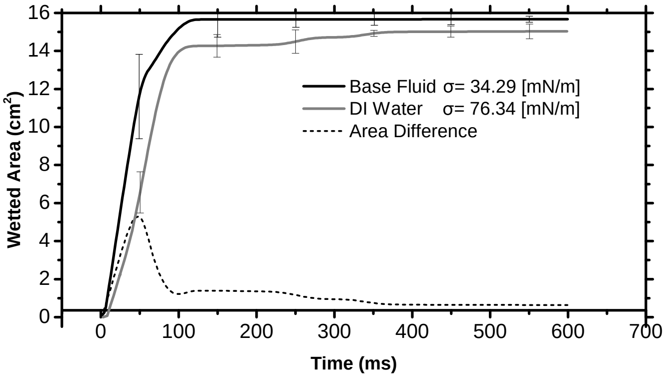

Figure 4.20: Effect of surface tension on the wetted area between different liquids (T_0=145°C, Z=20mm)

4.3.6 Effect of adding nanoparticles

Finally, the addition of nanoparticles will be discussed. First, the nanofluids will be compared while increasing nanoparticle concentration, then changing their geometry and base material, using one set of conditions ($Z = 20\ mm$ and $T_0 = 145°C$). Then a final comparison between fluids with and without nanoparticles will be presented.

4.3.6.A Effect of Nanoparticles Concentration

Figure 4.21 shows the transient cooling curves for three different concentrations of Gold spherical nanoparticles. From table 3.1, it is expected that liquids with higher nanoparticle concentration should increase the cooling performance. However, this was not observed for this range of concentration, as the highest gold concentration performed the worst relative to the lower concentrations. This discrepancy may be attributed to spray or nanofluid instability.

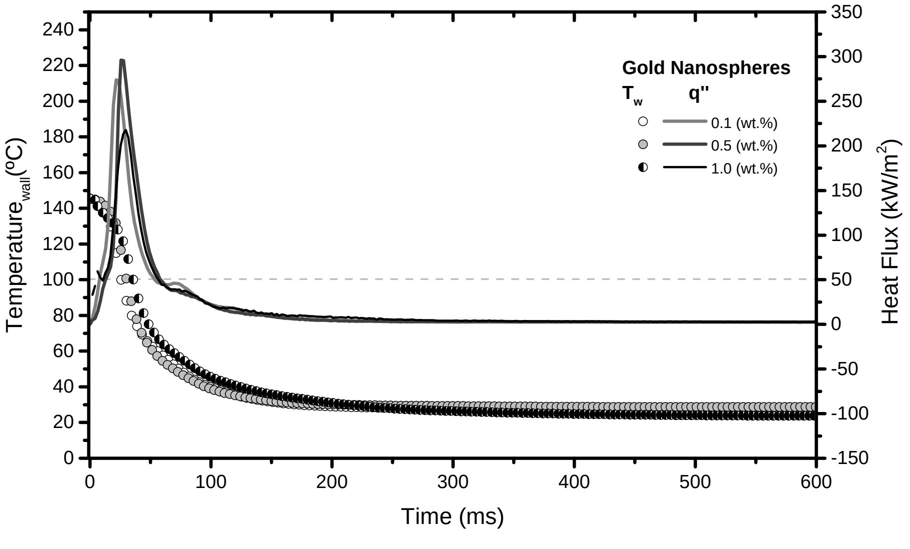

Figure 4.21: Transient cooling curves of gold nanofluids with different concentration

Between the lowest concentrations, the one with 0.5(wt.%) performed better, achieving a maximum heat flux of 295.9 kW/m^2. Nevertheless, this value is only 7.7% higher than the one for 0.1 (wt.%). Overall, the concentration dependence is not significant within the 0.1 - 1 (wt.%) range.

4.3.6.B Effects of nanoparticle geometry and material

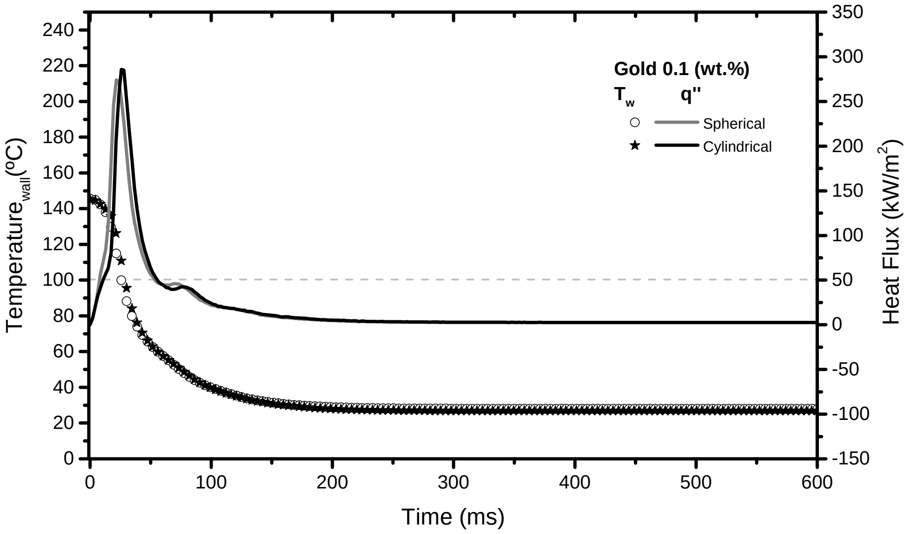

Figure 4.22: Transient cooling curves for gold nanofluids with different geometries

Comparing different geometries of gold nanoparticles with the same concentration, from Figure 4.22 no differences are observed. This suggests that nanoparticle geometry does not play a major influence on heat transfer, at least for this set of conditions. The same is observed when changing the nanoparticle base material from gold to silver 0.5(wt.%), represented in Figure 4.23, showing no influence on heat removal. The comparable cooling performance between the two materials is consistent with their similar thermal properties (table 3.1).

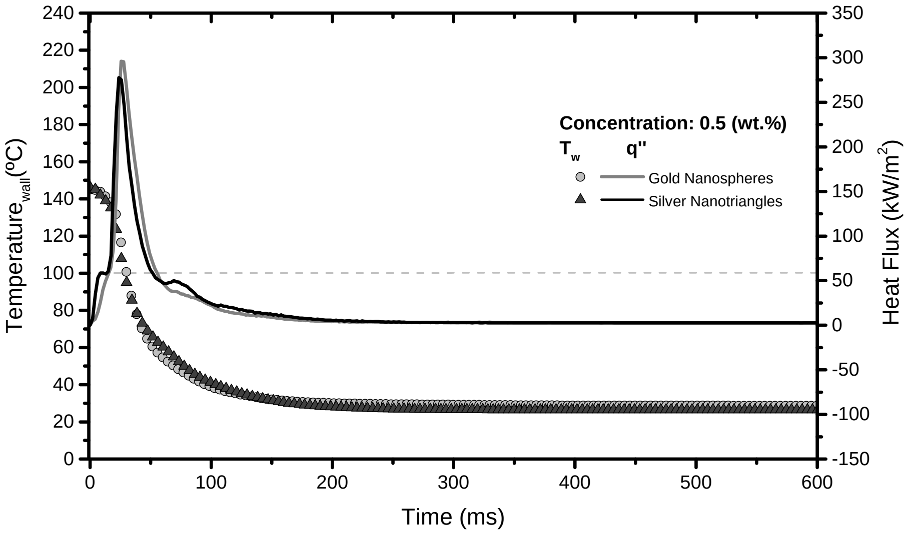

Figure 4.23: Transient cooling curves for silver and gold nanofluids at the same concentration

4.3.6.C Nanofluid and base liquid comparison

After comparing the nanofluids with each other, now a comparison between nanofluids and their base liquid and DI Water will be performed.

Figure 4.24 shows the transient variation of the space averaged temperature, and one can state that nanofluids follow the same profile of the base liquid. Nevertheless, the nanofluids achieve a lower temperature within the first 50 ms. This will translate in higher removed heat fluxes from the wall within that interval, suggesting that the addition of nanoparticles (from the exception of gold with 1 (wt.%)) enhances the thermal response when compared with the base fluid.

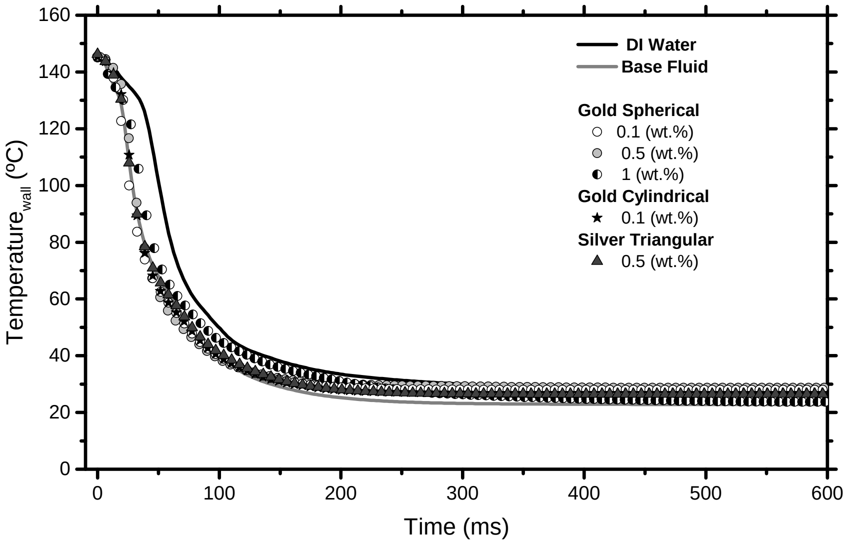

Figure 4.24: Transient variation of the space averaged surface temperature

As Figure 4.25 shows, the nanoparticles increased the maximum removed heat flux from the wall at higher temperatures (from $110.8 - 116.6\ ^{\circ}C$), enhancing cooling performance.

Performing a comparison between nanofluids and DI Water, differences are evident. The heat fluxes are lower for DI Water, whose maximum value is given at a lower temperature ($105\ ^{\circ}C$). Overall. the reason for these differences lye under two major dynamic changes:

- Spray dynamics – the lower surface tension caused by the addition of the surfactant promotes the liquid sheet breakup, enhancing the droplet formation and the spray radial expansion, which in turn increased the maximum heat flux;
- Liquid thermal dynamics – the surfactant increases the surface wettability that promotes the liquid-surface contact, and the nanoparticle addition improves the liquid's thermal conduction (in theory), which slightly enhanced the maximum heat flux.

Therefore, the superposition of these two existing dynamics is responsible for the higher cooling performance of the base fluid and consequently of the nanofluids, as opposed to the DI water. These mechanisms will translate to lower heat transfer coefficients at higher temperatures or on the initial contact with the surface for the DI water spray.

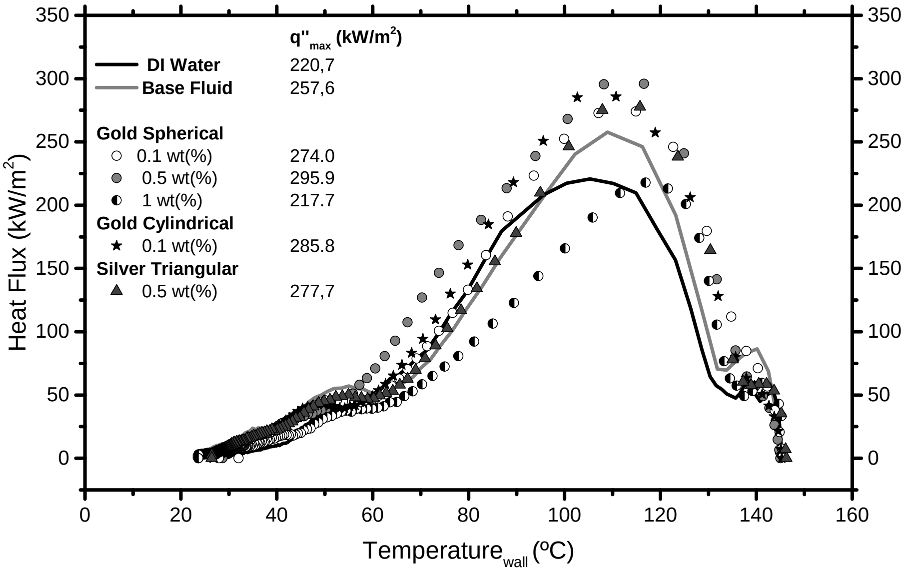

Figure 4.25: Variation of the overall space averaged heat flux with the space averaged surface temperature

Moreover, when computing the heat transfer coefficient as $h = q''_w/(T_w - T_f)$ with $T_f\ = 20\ ^{\circ}C$, one can calculate the ratios of h_{nf}/h_{BF} or h_{nf}/h_{DW} for different wall temperatures. Figure 4.26(a) and Figure 4.26(b), represents those ratios for the same wall temperature, interpolating the removed heat flux.

It is worth mentioning that the results plotted in Figure 4.26 should be interpreted with caution

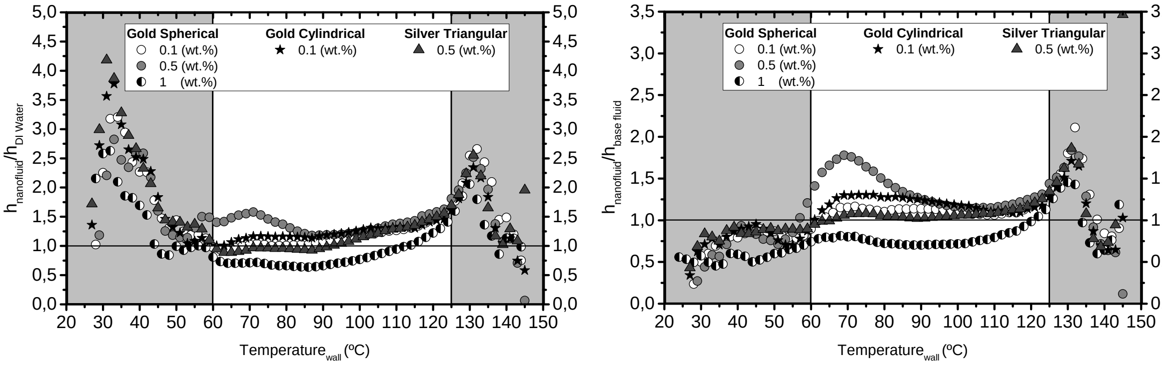

(a) DI Water

(b) Base Fluid

Figure 4.26: Heat transfer coefficient ratio between the different nanofluids compared to their base fluid and DI Water

since the initial heat transfer coefficient ratios at higher temperatures are sensible to spray randomness and interpolation errors. Therefore, the initial and final values, depicting the largest errors, were not considered for this analysis. With this in mind, the nanofluids showed an overall higher heat transfer coefficient when compared to water and the base fluid (water and CTAB). Hence, the maximum heat transfer coefficients obtained for the nanofluids (at the exception of gold 1 (wt.%)) can be 9.8% to 21.9% higher when compared to those obtained with the base fluid and 11.5% to 38.8% higher when compared with those obtained with DI water.

5

Conclusions and Recommendations

Contents

5.1 Conclusions

The study carried out through this dissertation aimed at describing the heat transfer phenomena during nanofluid spray impingement. To this end, several nanofluids were atomized, taking advantage of their superior thermodynamic properties, inferring the effect of different nanoparticle chemical element, geometry and concentration on the spray cooling dynamics.

In a first analysis, the thermophysical properties of the fluids under study were measured and some were computed adopting a classical approach. Additionally, the HS camera was used to compute the spray cone angle, whose measurements were used to dimensionalize the impact surface.

The effects of the parameters under study on the droplet size and velocity distribution were analyzed using a phase Doppler system. It was verified that surface tension plays a dominant role in the atomization process. Its decrease reduced the overall droplet size and increased the droplet generation rate. This decreased the mean Reynolds number and increased the Weber number, that increases the Ohnersorge number. However, the addition of nanoparticles in the base fluid did not modify the atomization process within the tested conditions. This is a positive indicator, meaning that any differences regarding the cooling performance can be only attributed to heat transfer dynamics at the liquid-solid surface interface.

As the PDA system was used with the free spray, the possible impact outcomes were qualitatively analysed, using empirical impact thresholds. Nevertheless, nanoparticles did not influence the impact outcome predictions when compared to the base fluid.

Afterwards, the experimental installation was adapted to accommodate a heated thin stainless-steel surface, used for impact. A high-speed time-resolved IR camera was placed beneath it to detail the heat transfer and to explore its use to describe such complex phenomena. This analysis was performed with a custom-made calibration and with a MATLAB routine, which was adapted from pool boiling to spray impact. According to the results, this method proved to be reliable as it captured details of the temperature variations from spray impingement. It should also be pointed out that the results were repeatable, mainly attributed to the use of the solenoid valve. Moreover, the IR camera and the HS camera were actuated simultaneously. Their synchronization was helpful to verify the spray actuation repeatability and to examine possible heat transfer phenomena (e.g. nucleate boiling, droplet evaporation). However, in the tested conditions, these mechanisms were absent.

In this order, the cooling experiments were conducted. As the surface-to-nozzle distance increased from 10 to 20 mm, the heat flux increased. This is mainly attributed to the increased wetted area at a higher surface to nozzle distance. The initial temperature influence was also analyzed, however, the surface was not hot enough to change the heat transfer mechanisms. Therefore, only single-phase heat transfer was attained. In those conditions, the removed heat flux increased as the initial temperature increased, as expected.

Furthermore, liquids with lower surface tension enhanced the transient evolution of the wetted area.

This is associated with the decreased droplet contact angle during impact and with the atomization enhancement, which in turn promoted the maximum removed heat flux. Regarding the addition of nanoparticles, the lowest concentrations of gold nanospheres enhanced the maximum averaged heat flux, which in turn increased the heat transfer coefficient. The opposite was obtained with the highest gold nanospheres concentration. Changing the geometry of the gold nanoparticles, from spheres to cylinders, did not express any main differences in HT. The same result was obtained for different nanoparticle elements. This shows that these parameters do not influence HT for this set of concentrations and conditions.

To summarize, the present study included an overview of important parameters that influence the spray cooling, with and without nanoparticles. A novel experimental methodology resulting from the combination of different techniques was adopted. It should be noted that this methodology allows for different analysis and comparisons. This methodology also promises to be helpful for the development of future numerical studies.

It should be pointed out that part of this dissertation was accepted at the 20th International Symposium on Applications of Laser and Imaging Techniques to Fluid Mechanics 2020, Lisbon, Portugal (canceled due to Covid-19 pandemic restriction measures).

5.2 Recommendations and Future Work

Regarding future studies, there are many possibilities for complementing and improve the present one. The range of nanoparticle chemical element and nanoparticle concentrations should be increased, hopefully allowing for considerate thermophysical changes on the base fluid.

Improvements to the impingement surface should be adopted, to decrease the corrugation effect of the stainless steel sheet, and heat losses from the surface to the support should be eradicated (diminishing temperature variations at the black painted area edges). Moreover, the imposed heat flux should be increased, to reach a higher initial surface temperature, which in turn could trigger the nucleate boiling and possibly the film boiling regime. For those cases, it would be interesting to analyze the impingement surface before and after use, to check for nanoparticle deposition and nano-sorption layer formation, that are addressed in the literature.

Finally, the synchronization of the three systems used in this study would be vital, not only to quantify the real impact outcomes of the droplets but also to compare the removed heat flux with the impinging mass flux. Again, this would facilitate the development of future correlations, that in turn would be useful for numerical studies.

Bibliography

[1] G. Liang and I. Mudawar, "Review of spray cooling–part 1: Single-phase and nucleate boiling regimes, and critical heat flux," *International Journal of Heat and Mass Transfer*, vol. 115, pp. 1174–1205, 2017.

[2] A. H. Lefebvre and V. G. McDonell, *Atomization and sprays.* CRC press, 2017.

[3] A. Moreira, A. Moita, and M. Panao, "Advances and challenges in explaining fuel spray impingement: How much of single droplet impact research is useful?" *Progress in energy and combustion science*, vol. 36, no. 5, pp. 554–580, 2010.

[4] *Dantec Dynamics*, https://www.dantecdynamics.com/solutions-applications/solutions/spray-and-particle/phase-doppler-anemometry-pda/ (accessed: March 2020).

[5] J. Kim, "Spray cooling heat transfer: The state of the art," *International Journal of Heat and Fluid Flow*, vol. 28, no. 4, pp. 753–767, 2007.

[6] R.-H. Chen, L. C. Chow, and J. E. Navedo, "Effects of spray characteristics on critical heat flux in subcooled water spray cooling," *International Journal of Heat and Mass Transfer*, vol. 45, no. 19, pp. 4033–4043, 2002.

[7] M. Malỳ, A. Moita, J. Jedelsky, A. Ribeiro, and A. Moreira, "Effect of nanoparticles concentration on the characteristics of nanofluid sprays for cooling applications," *Journal of Thermal Analysis and Calorimetry*, vol. 135, no. 6, pp. 3375–3386, 2019.

[8] S. Murshed, K. Leong, and C. Yang, "Thermophysical and electrokinetic properties of nanofluids–a critical review," *Applied Thermal Engineering*, vol. 28, no. 17-18, pp. 2109–2125, 2008.

[9] M. Roudini and G. Wozniak, "Investigation of the secondary atomization in prefilming air-blast atomizers," *International Journal of Chemical Engineering and Applications*, vol. 10, no. 5, pp. 138–143, 2019.

[10] S.-S. Hsieh, H.-Y. Leu, and H.-H. Liu, "Spray cooling characteristics of nanofluids for electronic power devices," *Nanoscale research letters*, vol. 10, no. 1, p. 139, 2015.

[11] M. Gupta, V. Singh, R. Kumar, and Z. Said, “A review on thermophysical properties of nanofluids and heat transfer applications,” *Renewable and Sustainable Energy Reviews*, vol. 74, pp. 638–670, 2017.

[12] Y. Gan and L. Qiao, “Evaporation characteristics of fuel droplets with the addition of nanoparticles under natural and forced convections,” *International Journal of Heat and Mass Transfer*, vol. 54, no. 23-24, pp. 4913–4922, 2011.

[13] Z. Yan, R. Zhao, F. Duan, T. N. Wong, K. C. Toh, K. F. Choo, P. K. Chan, and Y. S. Chua, “Spray cooling,” in *Two Phase Flow, Phase Change and Numerical Modeling.* IntechOpen, 2011.

[14] K. A. Estes and I. Mudawar, “Correlation of sauter mean diameter and critical heat flux for spray cooling of small surfaces,” *International Journal of Heat and Mass Transfer*, vol. 38, no. 16, pp. 2985–2996, 1995.

[15] W.-L. Cheng, F.-Y. Han, Q.-N. Liu, and H.-L. Fan, “Spray characteristics and spray cooling heat transfer in the non-boiling regime,” *Energy*, vol. 36, no. 5, pp. 3399–3405, 2011.

[16] J. Philip and P. D. Shima, “Thermal properties of nanofluids,” *Advances in colloid and interface science*, vol. 183, pp. 30–45, 2012.

[17] T.-B. Chang, S.-C. Syu, and Y.-K. Yang, “Effects of particle volume fraction on spray heat transfer performance of al2o3–water nanofluid,” *International Journal of Heat and Mass Transfer*, vol. 55, no. 4, pp. 1014–1021, 2012.

[18] S. V. Ravikumar, K. Haldar, J. M. Jha, S. Chakraborty, I. Sarkar, S. K. Pal, and S. Chakraborty, “Heat transfer enhancement using air-atomized spray cooling with water–al2o3 nanofluid,” *International Journal of Thermal Sciences*, vol. 96, pp. 85–93, 2015.

[19] N. Ashgriz, *Handbook of atomization and sprays: theory and applications.* Springer Science & Business Media, 2011.

[20] C. Bai and A. Gosman, “Development of methodology for spray impingement simulation,” *SAE transactions*, pp. 550–568, 1995.

[21] C. Bai, H. Rusche, and A. Gosman, “Modeling of gasoline spray impingement,” *Atomization and Sprays*, vol. 12, no. 1-3, 2002.

[22] R. Rioboo, C. Tropea, and M. Marengo, “Outcomes from a drop impact on solid surfaces,” *Atomization and sprays*, vol. 11, no. 2, 2001.

[23] A. Moita and A. Moreira, “Experimental study on fuel drop impacts onto rigid surfaces: Morphological comparisons, disintegration limits and secondary atomization,” *Proceedings of the combustion institute*, vol. 31, no. 2, pp. 2175–2183, 2007.

[24] C. D. Stow and M. G. Hadfield, “An experimental investigation of fluid flow resulting from the impact of a water drop with an unyielding dry surface,” *Proceedings of the Royal Society of London. A. Mathematical and Physical Sciences*, vol. 373, no. 1755, pp. 419–441, 1981.

[25] C. Mundo, M. Sommerfeld, and C. Tropea, “Droplet-wall collisions: experimental studies of the deformation and breakup process,” *International journal of multiphase flow*, vol. 21, no. 2, pp. 151–173, 1995.

[26] ——, “On the modeling of liquid sprays impinging on surfaces,” *Atomization and sprays*, vol. 8, no. 6, 1998.

[27] T. L. Bergman, F. P. Incropera, D. P. DeWitt, and A. S. Lavine, *Fundamentals of heat and mass transfer*. John Wiley & Sons, 2011.

[28] A. Sielaff, “Experimental investigation of single bubbles and bubble interactions in nucleate boiling,” Ph.D. dissertation, Technische Universität, 2014.

[29] P. Pontes, “Thermographical analysis of interface heat transfer mechanisms, with high temporal resolution,” Master’s thesis, Universidade de Lisboa Instituto Superior Técnico, 2016.

[30] W. Qi, M. Wang, and Q. Liu, “Shape factor of nonspherical nanoparticles,” *Journal of materials science*, vol. 40, no. 9-10, pp. 2737–2739, 2005.

[31] A. Fantoni, M. Fernandes, Y. Vygranenko, P. Louro, M. Vieira, R. Silva, D. Texeira, A. Ribeiro, M. Prazeres, and E. Alegria, “Analysis of metallic nanoparticles embedded in thin film semiconductors for optoelectronic applications,” *Optical and Quantum Electronics*, vol. 50, no. 6, p. 246, 2018.

[32] *HyperPhysics Thermodynamics*, http://hyperphysics.phy-astr.gsu.edu/hbase/Tables/thrcn.html (accessed: March 2020).

[33] *BSA Flow Software Users Guide*. DANTEC DYNAMICS, 2012.

[34] R. Cautela, “Descrição dos mecanismos de ebulição em meio quiescente usando superfícies bifílicas,” Master’s thesis, Universidade de Lisboa Instituto Superior Técnico, 2019.

[35] S.-S. Hsieh, H.-H. Liu, and Y.-F. Yeh, “Nanofluids spray heat transfer enhancement,” *International Journal of Heat and Mass Transfer*, vol. 94, pp. 104–118, 2016.

[36] J.-H. Lee, K. S. Hwang, S. P. Jang, B. H. Lee, J. H. Kim, S. U. Choi, and C. J. Choi, “Effective viscosities and thermal conductivities of aqueous nanofluids containing low volume concentrations of al2o3 nanoparticles,” *International Journal of Heat and Mass Transfer*, vol. 51, no. 11-12, pp. 2651–2656, 2008.

[37] M. Panão, “Experiments on impinging intermittent sprays: Dynamic behaviour of impact,” Ph.D. dissertation, Universidade Técnica de Lisboa Instituto Superior Técnico, 2009.

[38] A. Labergue, M. Gradeck, and F. Lemoine, “Comparative study of the cooling of a hot temperature surface using sprays and liquid jets,” *International Journal of Heat and Mass Transfer*, vol. 81, pp. 889–900, 2015.